Petroleum Science 23 (2026) 524–540

Contents lists available at ScienceDirect

Petroleum Science

journal homepage: www.keaipublishing.com/en/journals/petroleum-science

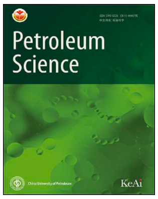

Original Paper

Development of an innovative permeability model for hydrate-bearing sediments under creep conditions: Effects of particle shape and non-uniform particle distribution

Yi-Han Shang [a,b], Gang Lei [a,b,*], Xiao-Yu Yuan [a,b], Ke-Yi Wang [a,b], Kai-Xuan Qiu [c,**]

[a] Institute for Advanced Marine Research, China University of Geosciences, Guangzhou, 511462, Guangdong, China
[b] National Center for International Research on Deep Earth Drilling and Resource Development, Faculty of Engineering, China University of Geosciences, Wuhan, 430074, Hubei, China
[c] Faculty of Engineering, Great Bay University, Dongguan, 523808, Guangdong, China

ARTICLE INFO

Article history:
Received 28 April 2025
Received in revised form
3 July 2025
Accepted 6 November 2025
Available online 13 November 2025

Edited by Teng Zhu

Keywords:
Hydrate-bearing sediments
Permeability
Creep
Non-uniform particle distribution
Particle shape
Hydrate pore morphology

ABSTRACT

Prolonged gas hydrate exploitation induces reservoir creep, leading to pore structure deformation, permeability reduction, and elevated risks of wellbore instability, ultimately impeding sustainable resource recovery. Accurate modeling of permeability evolution in hydrate-bearing sediments (HBS) under creep conditions is therefore crucial. However, the non-uniform distribution and irregular morphology of sediment particles complicate pore structures and fluid pathways, posing significant challenges for prediction. This study proposes a novel theoretical permeability model for HBS that incorporates the degree of non-uniform particle distribution, particle shape, pore structure creep, hydrate saturation, and hydrate pore morphology. Model validation against public datasets confirms its predictive capability. Sensitivity analysis reveals that pore structure creep, the degree of non-uniform particle distribution, and particle shape significantly influence permeability, with increased non-uniformity or larger particle aspect ratios leading to reduced permeability. For instance, after 40 h of creep, permeability decreases from 5 to 1.3 mD as the damage-related parameter β increases from 0.4 to 1.0. The proposed model advances understanding of permeability evolution in HBS and provides a theoretical basis for the long-term development of natural gas hydrates.

1. Introduction

Natural gas hydrate (NGH) holds great potential as an alternative energy source, offering extensive reserves found primarily in marine sediments and permafrost regions (Li et al., 2018; Ren et al., 2020; Liu and Li, 2021). With global natural gas consumption projected to increase by 44% by 2040 (Mao et al., 2024), NGH is receiving increasing attention for its potential to meet future energy demands (Gajanayake et al., 2023; Li et al., 2023). During the development of NGH, permeability is a crucial physical parameter that directly influences mass transfer, hydrate formation, solid migration, sediment deformation, and gas production efficiency (Lai et al., 2018; Liu et al., 2024).

Depressurization is an effective technique for extracting natural gas hydrates from sediment pore spaces (Yoneda et al., 2019). The low pore pressure induced by depressurization increases the effective stress, leading to compaction behavior of sediments in the initial stage of extraction (Zhang et al., 2024b; Ouria, 2024). When depressurized to the target pressure and maintained stable, the effective stress tends to be constant, and long-term hydrate extraction at this point triggers creep in hydrate-bearing sediments (HBS) (Li et al., 2019). Such creep compresses the pore spaces for fluid flow, resulting in reduced permeability and ultimately decreasing natural gas production (Chen et al., 2023; Hu et al., 2025). Therefore, understanding how creep affects permeability evolution in HBS is essential for sustainable and efficient NGH extraction. Since permeability not only characterizes the fluid flow capacity in HBS, but also reflects the complexity of the sediment's pore structure (Liu and Jeng, 2019;

---

* Corresponding author.
** Corresponding author.
E-mail addresses: leigang@cug.edu.cn (G. Lei), qiukx@gbu.edu.cn (K.-X. Qiu).

Peer review under the responsibility of China University of Petroleum (Beijing).

https://doi.org/10.1016/j.petsci.2025.11.018

Zhang et al., 2022), it is influenced by various factors under HBS creep (Ren et al., 2020). For example, the non-uniform distribution of sediment particles, which induces spatial variations in particle spacing (Bhade and Phirani, 2015; Liu et al., 2016), directly affects fluid flow capacity (Hafez et al., 2021) and thereby emerges as a key determinant of permeability (Peng et al., 2024). As permeability primarily depends on the geometric characteristics of the porous medium (Liu and Jeng, 2019), particle shape also can significantly influences fluid flow within the sediment (Tickell and Hiatt, 1938; Li et al., 2023; Song et al., 2024). Additionally, extensive triaxial creep experiments (Miyazaki et al., 2011, 2017; Li et al., 2019; Chen et al., 2023) have demonstrated that the effective stress greatly influences the mechanical behavior of HBS. Specifically, at low stress levels, the creep of HBS shows strong time dependence, and when the stress surpasses the sample's strength, HBS will directly collapse (Miyazaki et al., 2017). Other factors such as hydrate saturation (Wu et al., 2022; Zhang et al., 2022; Cheng et al., 2023) and hydrate pore morphology (Katagiri et al., 2017; Lv et al., 2021; Wang et al., 2021) also have non-negligible effects on permeability. Therefore, accurately predicting permeability changes requires a comprehensive consideration of these vital factors (i.e., the degree of non-uniform particle distribution, particle shape, pore structure creep, hydrate saturation, and hydrate pore morphology) on permeability of HBS.

Until now, many scholars have studied the relationship between hydrate saturation, hydrate pore morphology, and HBS permeability (Li et al., 2014; Mahabadi et al., 2019; Lv et al., 2021; Wang et al., 2021, 2025). To further study the fundamental mechanisms influencing the permeability of HBS, some experimental and theoretical studies have been carried out to explore the influence of the degree of non-uniform particle distribution (Peng et al., 2024), particle shape (Liu and Jeng, 2019; Yang and Chu, 2024), and pore structure creep on the permeability of HBS (Li et al., 2016, 2019; Cai et al., 2020; Wang et al., 2024). For example, based on Lattice Boltzmann method and Discrete Element method, Liu and Jeng (2019), Yang and Chu (2024) studied the impact of particle shape on HBS permeability, respectively. Li et al. (2024) proposed a permeability prediction model for complex geological conditions in the deep waters of the South China Sea using machine learning methods. Peng et al. (2024) developed a permeability model using vertical and horizontal particle distances to characterize the degree of non-uniform sediment particles. Their study suggest that non-uniform sediment particles distribution will significantly affect permeability of HBS. Although these studies can effectively study the impact of sediment particle shape and non-uniform distribution on permeability of HBS, they have not investigated the permeability of HBS under creep. Additionally, to better understand the permeability behavior of HBS under creep, Cai et al. (2020) conducted long-term water flow experiments on clay-silt sediment samples under stress conditions, and corroborated that the compression of pore and throat spaces in HBS accumulated as time increased. Besides experimental methods, theoretical models can also provide critical perspectives on the mechanisms of HBS permeability changes under creep effects (Lei et al., 2020; Li et al., 2022; Qu et al., 2025). For example, by combining a three-dimensional nonlinear creep constitutive equation and the KC equation, Zhang et al. (2020) proposed a fractional-order permeability model to characterize permeability of porous media at different creep stages. Recently, using nonlinear creep damage constitutive models (Liu et al., 2020; Hu et al., 2023; Sun et al., 2024), Lei et al. (2024a) and Qu et al. (2025) proposed permeability models to study the permeability change of HBS during creep. However, these theoretical models neglect the degree of non-uniform particle distribution (Kou et al., 2022; Song et al., 2024; Yang and Chu, 2024), and simplify sediment particles to spherical particles (Peng et al., 2024), which can introduce errors into permeability prediction. Thus, to more accurately predict the permeability behavior of HBS, more reliable permeability models should be established that incorporate creep, the non-uniform distribution and shape of sediment particles.

In this work, an innovative theoretical model is developed to predict HBS permeability under creep conditions, considering factors such as the degree of non-uniform particle distribution, particle shape, pore structure creep, hydrate saturation and hydrate pore morphology. Publicly available experimental results are used to verify the developed model. A parameter sensitivity analysis is then performed to assess the effect of key parameters (specifically, non-uniform parameter, particle aspect ratio, effective stress, dimensionless creep parameter and damage-related parameter) on permeability during creep. This derived model can precisely forecast HBS permeability evolution during long-term NGH extraction, providing theoretical support for mitigating wellbore instability risks, improving development efficiency, and optimizing extraction strategies.

2. Model development

2.1. Model assumptions

During the long-term extraction of NGH, stress loading causes time-dependent deformation of the sediment's pore structure (i.e., creep deformation) (Danesh et al., 2016; Guo et al., 2018). In this work, pore structures of HBS are characterized using the capillary bundle model (Fig. 1(a)) (Luo et al., 2023; Tang et al., 2024), which satisfy the fractal characteristics (Yu and Li, 2001; Yu and Cheng, 2002). The creep behavior of HBS is described by a nonlinear creep constitutive model (the details are shown in Fig. 2), in which the creep process is separated into three stages: decelerating creep, steady-state creep, and accelerating creep (Fig. 1(b)), where the emergence of accelerating creep marks the failure of HBS (Hu et al., 2023). This work focuses on grain-coating (GC) and pore-filling (PF) hydrates (Fig. 1(c)) in the pore space (Wang et al., 2021; Gao et al., 2024; Lei et al., 2024b; Tang et al., 2024). Additionally, the established permeability model complies with the following assumptions.

1. Under triaxial stress conditions, the radial stresses are assumed to be equal (i.e., $\sigma_2 = \sigma_3$) (Miyazaki et al., 2017; Sun et al., 2024), and the stress is uniformly distributed (Lei et al., 2024b; Zhang et al., 2024). A two-dimensional Euclidean space is used to develop the model.
2. Pore volume changes are due to the deformation of the skeleton and pores in HBS, with the deformation of sediment particles and hydrates neglected (Tang et al., 2023).
3. The pore space contains only GC hydrate, PF hydrate, and their mixed morphologies (Wang et al., 2021; Gao et al., 2024). The phase transition of hydrates is quantified by the variation in hydrate saturation, while complex kinetic and thermodynamic behaviors are not considered (Qu et al., 2024).
4. The sediment particles consist of ellipsoidal particles (Song et al., 2024), with their shape characterized by aspect ratio (Yang and Chu, 2024; Li et al., 2023). The degree of non-uniform distribution of particles in HBS is characterized by the non-uniform parameter m (the ratio of the horizontal distance to the vertical distance between adjacent sediment particles) and the offset angle θ (i.e., the angle between the center line of two adjacent particles and the flow direction) (Peng et al., 2024). In addition, m and θ remain constant during creep (Fig. 1(d)).

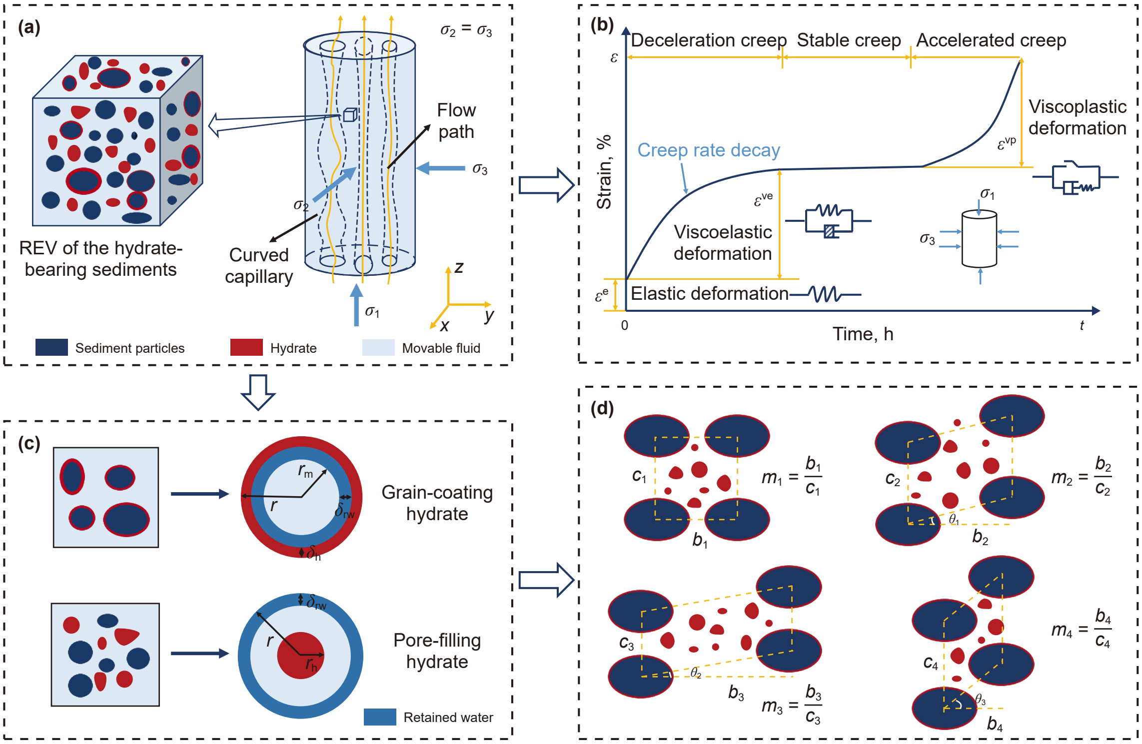

Fig. 1. Conceptual model of creep process of hydrate-bearing sediments under triaxial stress: **(a)** 3D structure of hydrate-bearing sediments; **(b)** General shape of creep curve of HBS sample; **(c)** Morphology of GC and PF hydrates; **(d)** Non-uniform distribution of sediment particles.

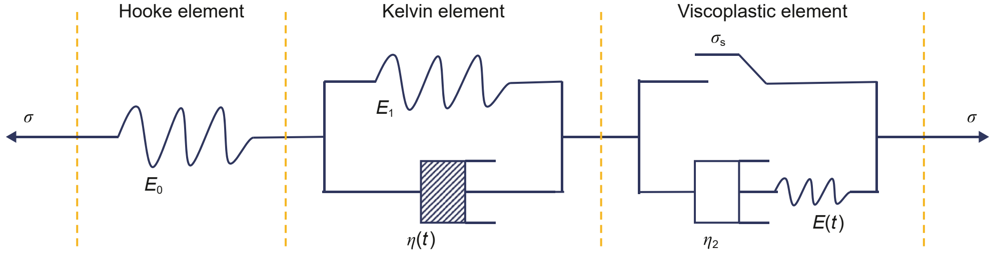

Fig. 2. Schematic of the nonlinear creep damage constitutive model of HBS.

2.2. Model derivation

The sediment skeleton consists of solid particles and hydrates (Lin et al., 2019), and provided the initial values of porosity φ_0 and hydrate saturation S_{h0} for HBS, the initial effective porosity φ_e is determined by (Lei et al., 2020; Qu et al., 2024)

$$\varphi_e = \varphi_0 (1 - S_{h0}) \tag{1}$$

where φ_0 represents the initial porosity, φ_e represents the initial effective porosity, S_{h0} represents the initial hydrate saturation.

During creep, due to the effects of axial stress σ_1, the second principal stress σ_2, and the third principal stress σ_3, the sediment skeleton deforms over time, leading to compression of the pore space (Li et al., 2019). Thus, the porosity of hydrate-free sediments under creep conditions can be derived by

$$\varphi = \frac{V_p}{V_b} = \frac{(V_{p0} - \Delta V_p)/V_{b0}}{(V_{b0} - \Delta V_p)/V_{b0}} = \frac{\varphi_0 - \varepsilon_v}{1 - \varepsilon_v} \tag{2}$$

where V_p and V_b represent the pore volume and apparent volume of HBS under creep conditions respectively, V_{p0} and V_{b0} are the initial pore volume and apparent volume respectively, ΔV_p denotes the pore volume of change, ε_v is the volumetric strain.

For HBS, the porosity under creep conditions can be determined by combining Eq. (1) and Eq. (2)

$$\varphi = \frac{\varphi_0 (1 - S_{h0}) - \varepsilon_v}{1 - \varepsilon_v} \tag{3}$$

Assuming the total volume of hydrates remains constant during creep (Qu et al., 2025), the hydrate saturation S_h under creep conditions is calculated by

$$S_h = \frac{V_{p0} S_{h0}}{V_p} = \frac{V_{p0} S_{h0}}{V_{p0} - \Delta V_p} = \frac{S_{h0}}{1 - \Delta V_p / V_{p0}} \tag{4}$$

where $\Delta V_p / V_{p0}$ can be determined by the following equation

$$\varphi = \frac{(V_{p0} - \Delta V_p)/V_{p0}}{(V_{b0} - \Delta V_p)/V_{p0}} = \frac{1 - \Delta V_p / V_{p0}}{1/\varphi_0 - \Delta V_p / V_{p0}} \Rightarrow \frac{\Delta V_p}{V_{p0}} = \frac{1 - \varphi/\varphi_0}{1 - \varphi} \tag{5}$$

By substituting Eq. (5) into Eq. (4), the hydrate saturation S_h is expressed as

$$S_{\mathrm{h}} = \frac{\varphi_0(1-\varphi)S_{\mathrm{h}0}}{\varphi(1-\varphi_0)} \tag{6}$$

Hu et al. (2023) established a modified nonlinear creep damage constitutive model, derived from the Nishihara model (Yan et al., 2020), to accurately represent the creep behavior of HBS throughout the process. The modified model features a Hooke element, a Kelvin element and an ideal viscous element in series (Fig. 2), with the introduction of a nonlinear viscosity coefficient and an elastomer that takes into account the temporal damage to HBS, thereby describing the nonlinear creep characteristics of HBS. The steady-state creep stage is primarily governed by the Kelvin element, where H_1 denotes its three-dimensional viscosity coefficient of the modified Kelvin element. When the axial load exceeds the long-term strength σ_{s}, accelerating creep occurs, causing permanent damage to the HBS. The accelerating creep stage is primarily characterized by the viscoplastic element, with H_2 serving as the three-dimensional viscosity coefficient of the modified viscoplastic element.

According to the HBS creep model of Hu et al. (2023), the volumetric strain ε_{v} under three-dimensional stress condition, where the second and third principal stresses are equal, can be described as

$$\begin{cases} \varepsilon_{\mathrm{v}} = \dfrac{\sigma_1-\sigma_3}{3G_0} + \dfrac{\sigma_1+2\sigma_3}{9K_0} + \dfrac{\sigma_1-\sigma_3}{3G_1}\left\{1-\exp\left[-\dfrac{G_1\left(e^{at}-1\right)}{H_1 a}\right]\right\}, \sigma_1-\sigma_3<\sigma_{\mathrm{s}} \\ \varepsilon_{\mathrm{v}} = \left\langle \begin{aligned} &\dfrac{\sigma_1-\sigma_3}{3G_0} + \dfrac{\sigma_1+2\sigma_3}{9K_0} + \dfrac{\sigma_1-\sigma_3}{3G_1}\left\{1-\exp\left[-\dfrac{G_1\left(e^{at}-1\right)}{H_1 a}\right]\right\} \\ &+\dfrac{\sigma_1-\sigma_3-\sigma_{\mathrm{s}}}{3H_2}t + \dfrac{\sigma_1-\sigma_3-\sigma_{\mathrm{s}}}{3G_2}\exp\left(\dfrac{t}{t_1}\right)^{\beta} \end{aligned} \right\rangle, \sigma_1-\sigma_3\geq\sigma_{\mathrm{s}} \end{cases} \tag{7}$$

where σ_1, σ_2 and σ_3 are the axial stress, the second principal stress and the third principal stress, respectively; G_0 is the shear modulus for the Hooke element in MPa, K_0 is the bulk modulus for the Hooke element in MPa, G_1 is the shear modulus of the modified Kelvin element in MPa, G_2 is the shear modulus of the modified viscoplastic element in MPa, H_1 is the three-dimensional viscosity coefficient of the modified Kelvin element in MPa·h, H_2 is the three-dimensional viscosity coefficient of the modified viscoplastic element in MPa·h; a and β represent the dimensionless creep parameter, and the damage-related parameter, respectively; t and t_1 are the creep duration and the damage threshold time, respectively; σ_{s} denotes the long-term strength.

Porosity φ, hydrate saturation S_{h}, and volumetric strain ε_{v} of HBS under creep conditions can be obtained by Eqs. (3), (6) and (7) respectively. Based on the fractal theory and Eq. (B1), the pore fractal dimension under creep conditions is $D_{\mathrm{f}} = 2 - (\ln\varphi)/\ln(r_{\min}/r_{\max})$. Assuming that the specific surface area of HBS stays unchanged under creep conditions, the following equation is obtained (Lei et al., 2018a, 2018b, 2021).

$$\frac{3\left(3-D_{\mathrm{f}0}\right)}{4\left(2-D_{\mathrm{f}0}\right)}\frac{r_{\max0}^{2-D_{\mathrm{f}0}}-r_{\min0}^{2-D_{\mathrm{f}0}}}{r_{\max0}^{3-D_{\mathrm{f}0}}-r_{\min0}^{3-D_{\mathrm{f}0}}}=\frac{A_{\mathrm{p}0}}{V_{\mathrm{p}0}}=\frac{A_{\mathrm{p}}}{V_{\mathrm{p}}}=\frac{3\left(3-D_{\mathrm{f}}\right)}{4\left(2-D_{\mathrm{f}}\right)}\frac{r_{\max}^{2-D_{\mathrm{f}}}-r_{\min}^{2-D_{\mathrm{f}}}}{r_{\max}^{3-D_{\mathrm{f}}}-r_{\min}^{3-D_{\mathrm{f}}}} \tag{8}$$

where $r_{\max}$ and $r_{\min}$ are the maximum and minimum pore radius of HBS during creep respectively, $A_{\mathrm{p}0}$ represents the initial overall pore area in the cross-section of representative elementary volume (REV), A_{p} represents the overall pore area in the cross-section of REV during creep, D_{f} is the pore fractal dimension under creep.

By solving Eq. (8), the correlation between the initial maximum pore radius and the maximum pore radius under creep conditions of HBS can be given as

$$r_{\max} = r_{\max0}\left[\frac{\left(2-D_{\mathrm{f}0}\right)\left(3-D_{\mathrm{f}}\right)}{\left(2-D_{\mathrm{f}}\right)\left(3-D_{\mathrm{f}0}\right)}\right] \tag{9}$$

Since the minimum and maximum pore radius of HBS satisfy $r_{\min}/r_{\max} \leq 0.01$ (Du et al., 2020), the ratio is set to 0.01 to simplify the model in this study (Lei et al., 2020; Qu et al., 2025; Tang et al., 2024). Therefore, the cross-sectional area of REV can be calculated by

$$A = \frac{\pi D_{\mathrm{f}} r_{\max}^2}{2-D_{\mathrm{f}}}\left(\frac{r_{\max}^{2-D_{\mathrm{f}}}}{r_{\min}^{2-D_{\mathrm{f}}}}-1\right) \tag{10}$$

where A is the cross-sectional area of REV. Using Eq. (10), the capillary characteristic length L is given by $L=\sqrt{A}$.

The average tortuosity τ of HBS during creep can be calculated as

$$\begin{aligned}\tau = {}&\frac{1}{8}\left[1+\frac{1}{1-\sqrt{\dfrac{4m(1-\varphi)}{\pi}}}\right]\left[\begin{aligned}&\left(\pi\sqrt{\alpha}-2\theta-\sqrt{\frac{4\alpha}{\sin\theta^2+(\alpha\cos\theta)^2}}\right)\sqrt{\frac{\alpha m(1-\varphi)}{\pi}} \\ &+(1-\alpha)\sqrt{\frac{4m(1-\varphi)}{\pi}}+\frac{1}{\cos\theta}\end{aligned}\right]+ \\ &\frac{3}{8}\left[1+\frac{1}{1-\sqrt{\dfrac{4m(1-\varphi)}{\pi}}}\right]\sqrt{(\tan\theta)^2+\left(1-\alpha\sqrt{\frac{4m(1-\varphi)}{\left[(\cot\theta)^2+\alpha^2\right]\pi}}\right)^2}+\sqrt{\frac{\alpha m(1-\varphi)}{\pi}}\theta\end{aligned} \tag{11}$$

where τ represents average tortuosity of HBS (the detailed derivation of average tortuosity is shown in Appendix A), m represents non-uniform parameter, α is the aspect ratio of the ellipsoidal particles, θ is the offset angle.

Studies have shown that hydrate occurrence patterns can be divided into: pore-filling, grain-coating, cementing, load-bearing, and pathy (Ren et al., 2020). Nevertheless, accurately and comprehensively quantifying all hydrate morphologies is difficult. In addition, PF and GC hydrates are viewed as the two dominant hydrate growth patterns in HBS (Gao et al., 2024; Lei et al., 2024b; Qu et al., 2024; Tang et al., 2024). Therefore, this study primarily focuses on PF and GC hydrates, and the pore radius of HBS with GC and PF hydrates is determined by

$$\begin{cases} r_{\mathrm{GC}} = r\sqrt{1-S_{\mathrm{h}}} \\ r_{\mathrm{PF}} = r\left(1-\sqrt{S_{\mathrm{h}}}\right) \end{cases} \tag{12}$$

where r_{GC}, r_{PF} are the pore radius with GC hydrate and PF hydrate respectively.

According to Hagen-Poiseuille theory (Washburn, 1921; Yu, 2008), the flow rate through a single pipe of diameter λ is calculated by

$$q(\lambda) = \frac{\pi}{128}\frac{\Delta P}{L_{\mathrm{t}}}\frac{\lambda^4}{\mu} \tag{13}$$

where q is the flow rate through a single pipe, ΔP is the pressure drop across the tube, λ is the pore size of HBS, μ is the fluid dynamic viscosity, L_{t} is the actual length of the capillary, which can be calculated by Eq. (B3).

By adding up the flow rate from each pipe by combining Eq. (13) and Eq. (B5), the total flow through the REV cross-section of HBS with GC and PF hydrates can be determined by

$$\begin{cases} Q_{\mathrm{GC}} = -\displaystyle\int_{\lambda_{\min}\sqrt{1-S_{\mathrm{h}}}}^{\lambda_{\max}\sqrt{1-S_{\mathrm{h}}}} q(\lambda)\mathrm{d}N(\lambda) = \left\{ \begin{array}{l} \dfrac{\pi}{128}\dfrac{\Delta P}{\mu}\dfrac{L_0^{2-D_{\mathrm{T}}}D_{\mathrm{f}}}{3+D_{\mathrm{T}}-D_{\mathrm{f}}}\left(\lambda_{\max}\sqrt{1-S_{\mathrm{h}}}\right)^{3+D_{\mathrm{T}}} \\ \left[1-\left(\dfrac{\lambda_{\min}}{\lambda_{\max}}\right)^{3+D_{\mathrm{T}}-D_{\mathrm{f}}}\right] \end{array} \right\} \\ Q_{\mathrm{PF}} = -\displaystyle\int_{\lambda_{\min}\left(1-\sqrt{S_{\mathrm{h}}}\right)}^{\lambda_{\max}\left(1-\sqrt{S_{\mathrm{h}}}\right)} q(\lambda)\mathrm{d}N(\lambda) = \left\{ \begin{array}{l} \dfrac{\pi}{128}\dfrac{\Delta P}{\mu}\dfrac{L_0^{2-D_{\mathrm{T}}}D_{\mathrm{f}}}{3+D_{\mathrm{T}}-D_{\mathrm{f}}}\left[\lambda_{\max}\left(1-\sqrt{S_{\mathrm{h}}}\right)\right]^{3+D_{\mathrm{T}}} \\ \left[1-\left(\dfrac{\lambda_{\min}}{\lambda_{\max}}\right)^{3+D_{\mathrm{T}}-D_{\mathrm{f}}}\right] \end{array} \right\} \end{cases} \tag{14}$$

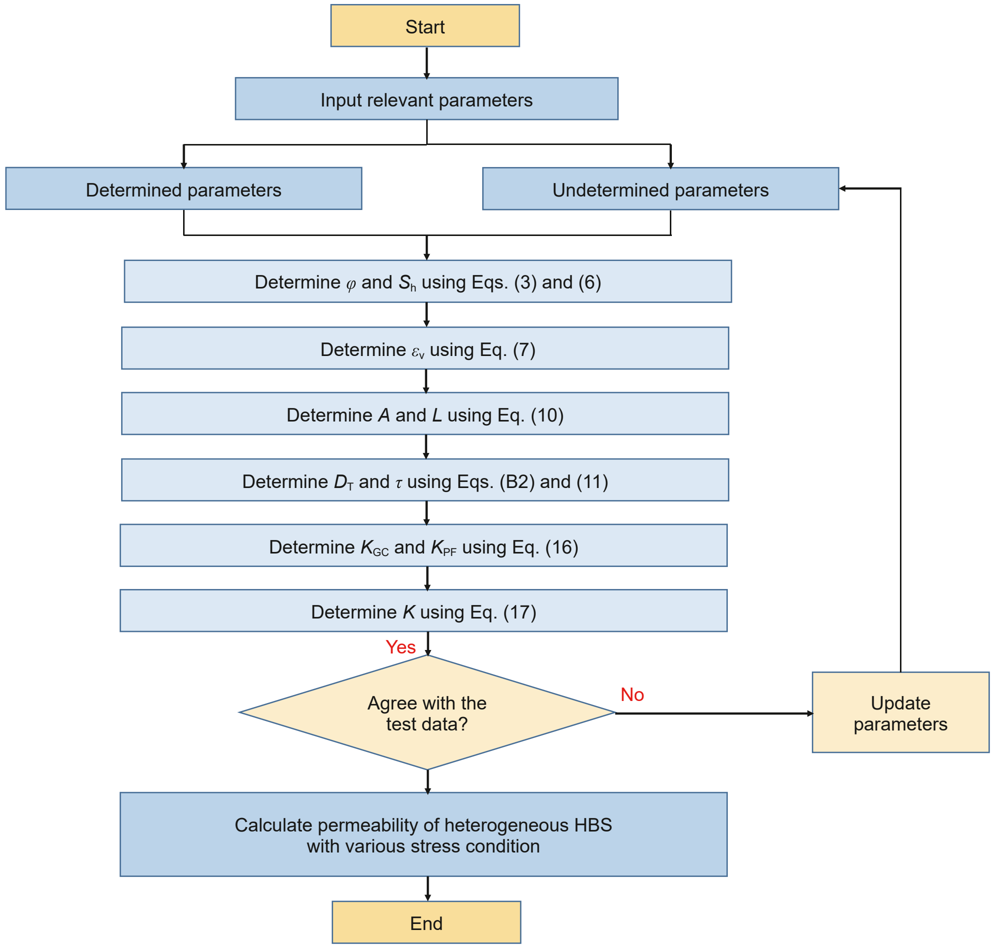

Fig. 3. Workflow of the proposed permeability model.

where Q_{GC} and Q_{PF} are the total flow through the REV cross-section of HBS with GC and PF hydrates respectively, D_{T} is the tortuosity fractal dimension, which can be obtained by Eq. (B2). Due to the Euclidean dimension is 2 in this work, we have $1 < D_{\mathrm{T}} < 2$, and $1 < D_{\mathrm{f}} < 2$ (Yu and Cheng, 2002). As mentioned before, $\lambda_{\min}/\lambda_{\max} = 0.01$, Eq. (14) can be simplified to

$$\begin{cases} Q_{\mathrm{GC}} = -\displaystyle\int_{\lambda_{\min}\sqrt{1-S_{\mathrm{h}}}}^{\lambda_{\max}\sqrt{1-S_{\mathrm{h}}}} q(\lambda)\mathrm{d}N(\lambda) = \frac{\pi}{128}\frac{\Delta P}{\mu}\frac{L_0^{2-D_{\mathrm{T}}}D_{\mathrm{f}}}{3+D_{\mathrm{T}}-D_{\mathrm{f}}}\left(\lambda_{\max}\sqrt{1-S_{\mathrm{h}}}\right)^{3+D_{\mathrm{T}}} \\ Q_{\mathrm{PF}} = -\displaystyle\int_{\lambda_{\min}\left(1-\sqrt{S_{\mathrm{h}}}\right)}^{\lambda_{\max}\left(1-\sqrt{S_{\mathrm{h}}}\right)} q(\lambda)\mathrm{d}N(\lambda) = \frac{\pi}{128}\frac{\Delta P}{\mu}\frac{L_0^{2-D_{\mathrm{T}}}D_{\mathrm{f}}}{3+D_{\mathrm{T}}-D_{\mathrm{f}}}\left[\lambda_{\max}\left(1-\sqrt{S_{\mathrm{h}}}\right)\right]^{3+D_{\mathrm{T}}} \end{cases} \tag{15}$$

According to Darcy's law (Lei et al., 2020), the permeability of HBS with GC and PF hydrates is given by

$$\begin{cases} K_{\mathrm{GC}} = \dfrac{\mu L_0 Q_{\mathrm{GC}}}{\Delta PA} = \dfrac{\pi}{128}\dfrac{L^{1-D_{\mathrm{T}}}}{A}\dfrac{D_{\mathrm{f}}}{3+D_{\mathrm{T}}-D_{\mathrm{f}}}\left(\lambda_{\max}\sqrt{1-S_{\mathrm{h}}}\right)^{3+D_{\mathrm{T}}} \\ K_{\mathrm{PF}} = \dfrac{\mu L_0 Q_{\mathrm{PF}}}{\Delta PA} = \dfrac{\pi}{128}\dfrac{L^{1-D_{\mathrm{T}}}}{A}\dfrac{D_{\mathrm{f}}}{3+D_{\mathrm{T}}-D_{\mathrm{f}}}\left[\lambda_{\max}\left(1-\sqrt{S_{\mathrm{h}}}\right)\right]^{3+D_{\mathrm{T}}} \end{cases} \tag{16}$$

where K_{GC} and K_{PF} represent the permeability of HBS with GC hydrate and PF hydrate respectively. Since the hybrid hydrate pore morphology is dominant in HBS in most cases (Wang et al., 2021), the transition saturation model proposed by Wang et al. (2021), which accounts for the combined effects of PF and GC hydrates morphologies, is adopted in this work to calculate the permeability of HBS

$$K = \left(K_{\mathrm{GC}}\right)^{1/\left[1+(S_{\mathrm{h}}/\gamma)^{\eta}\right]}\left(K_{\mathrm{PF}}\right)^{1-1/\left[1+(S_{\mathrm{h}}/\gamma)^{\eta}\right]} \tag{17}$$

where γ is transitional hydrate saturation, indicating the point at which the permeability of HBS begins to shift from one morphology-dominated mode to another, η represents the evolutionary direction of hydrate pore morphology: when the hydrate morphology transitions from GC to hybrid, η is positive; when the transition is from PF to hybrid morphology with increasing hydrate saturation, η is negative (Wang et al., 2021).

2.3. Workflow of permeability determination

As shown in Fig. 3, the procedure for permeability determination of HBS under creep conditions is outlined. The primary steps are listed below:

Step 1: Input the relevant parameters required by the permeability model, which are divided into determined and undetermined parameters. Determined parameters include initial porosity φ_0, initial hydrate saturation S_{h0}, initial maximum pore radius $r_{\max0}$, initial minimum pore radius $r_{\min0}$, the first principal stress σ_1, the second principal stress σ_2, the third principal stress σ_3, the shear modulus for the Hooke element G_0, the bulk modulus for the Hooke element K_0, the shear modulus of the modified Kelvin element G_1, the shear modulus of the modified viscoplastic element G_2, the three-dimensional viscosity coefficient of the modified Kelvin element H_1, the three-dimensional viscosity coefficient of the modified viscoplastic element H_2, the creep duration t, the damage threshold time t_1, the long-term strength σ_{s}. Undetermined parameters include the dimensionless creep parameter a, the damage-related parameter β, transitional hydrate saturation γ, the evolutionary direction of hydrate pore morphology η, the non-uniform parameter m, the offset angle θ, aspect ratio of ellipsoidal particles α. Notably, $r_{\max0}$ and $r_{\min0}$ may be considered undetermined parameters if they are hard to obtain.

Step 2: Parameters φ and hydrate saturation S_{h} under creep conditions can be obtained by Eqs. (3) and (6). The volumetric strain ε_{v} is calculated by Eq. (7).

Step 3: Then the REV cross-sectional area A and the capillary characteristic length L are calculated based on Eq. (10). And the tortuosity fractal dimension D_{T} and the average tortuosity τ under creep conditions are determined by Eqs. (B2) and (11).

Step 4: Permeability K_{GC} and K_{PF} can be calculated by Eq. (16). Finally, the permeability of HBS K is determined by Eq. (17). Undetermined parameters in this model should be updated when there is a discrepancy between the predicted results and the experimental data. The process is repeated until the predicted results align with the experimental data. Using the calibrated parameters with Eq. (17), the creep permeability of HBS under different stress conditions can be determined.

3. Results and discussion

3.1. Model validation

3.1.1. Verify the strain of HBS under creep conditions

As shown in Fig. 4, the creep strain calculated by Eq. (7) under varying stresses and initial hydrate saturations is compared with the experimental results measured by Sun et al. (2024). In 2024, Sun et al. (2024) performed triaxial compression creep experiments on hydrate-bearing sandy sediments with initial hydrate saturations of 20%, 30%, and 40% to investigate the creep characteristics of HBS under long-term high stress. According to their experimental conditions, the initial hydrate saturation, the effective porosity (0.388) of HBS, the long-term strength in HBS are determined to ensure consistency with the experimental materials. The acceptable range of creep parameters is adopted from Hu et al. (2023). Moreover, the following parameter values are used in our model: $m = 0.2$, $\theta = \pi/9$, $\alpha = 0.8$, $t_1 = 40$ h, $r_{\max0} = 3.91$ μm. Tables 1–3 summarize the parameter values used in these figures. Fig. 4 shows that the model's predicted strain closely aligns with experimental data, confirming its accuracy and effectiveness. The results in Fig. 4 indicate that, under triaxial loading conditions, when the axial stress is less than the long-term strength, the initial creep strain is relatively small, the creep rate decreases rapidly, and the HBS creep transitions into a stable creep phase. This suggests that the strain of HBS can remain stable under lower stress levels. When the axial stress surpasses the long-term strength, the creep curve transitions from the stable phase to the accelerated phase, during which the creep rate increases significantly. Notably, the long-term strength in HBS enhance from 2.2 to 3.4 MPa as the initial hydrate saturation increases from 20% to 40%. Furthermore, the strain of HBS during the accelerated creep phase decreases as hydrate saturation increases: $\varepsilon_{\mathrm{v}} = 6.07\%$ when $S_{\mathrm{h0}} = 20\%$ (Fig. 4(a)), $\varepsilon_{\mathrm{v}} = 4.77\%$ when $S_{\mathrm{h0}} = 30\%$ (Fig. 4(b)), and $\varepsilon_{\mathrm{v}} = 3.99\%$ when $S_{\mathrm{h0}} = 40\%$ (Fig. 4(c)). This phenomenon can be mechanistically explained by the load-bearing capacity of hydrate in HBS, where the hydrate provides structural support to the

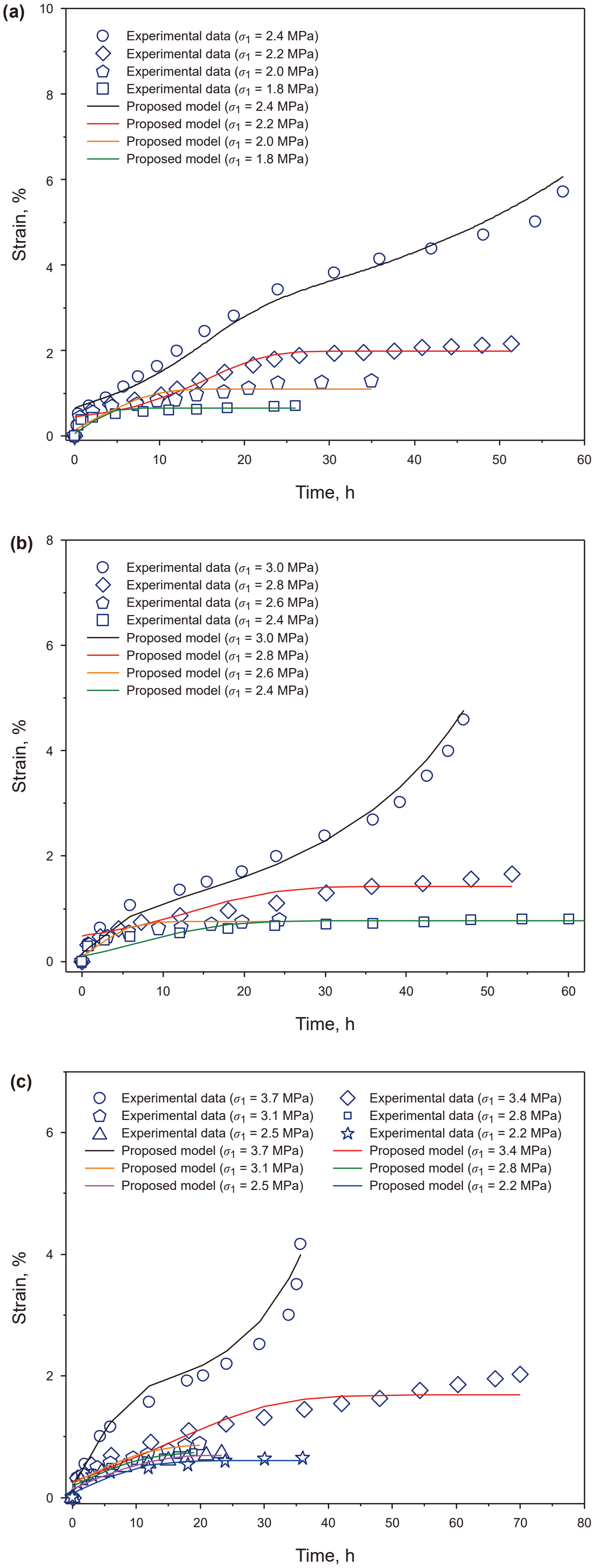

Fig. 4. Comparison of predicted strains with experimental data under different stresses and initial hydrate saturation: **(a)** $S_{h0} = 20\%$; **(b)** $S_{h0} = 30\%$; **(c)** $S_{h0} = 40\%$.

sediment framework, thereby enhancing its rigidity and strength (Qu et al., 2024; Wang et al., 2025).

3.1.2. Verify the permeability of HBS under creep conditions

The proposed model's predicted permeability is assessed in comparison with experimental data from Cai et al. (2020) (Fig. 5). By conducting the seepage experiments on HBS samples from gas hydrate reservoirs in the Shenhu area of the South China Sea, Cai et al. (2020) investigated the fundamental mechanism behind permeability change of HBS under creep. In the modeling setup, the reasonable range of the parameter values is obtained from Hu et al. (2023) and Wang et al. (2021), as shown in Table 4. Other key parameters are set as follows: $\varphi_0 = 0.33$, $S_{h0} = 31\%$, $m = 0.2$, $\theta = \pi/9$, $\alpha = 0.8$, $t_1 = 60$ h, $a = -6.06 \times 10^{-2}$, and $\beta = 3.94$. As illustrated in Fig. 5(a), the porosity predicted by our model matches well with the test data. In addition, Fig. 5(a) and (b) indicate that, when the axial stress increases from 10 to 100 kPa, porosity decreases from 18.6% to 11.2%, and permeability decreases from 13.44 to 3.51 mD. Moreover, Fig. 5(b) demonstrates that during the creep process, even under a constant axial stress, the permeability decreases continuously over time. Table 4 shows that the value of parameter η rises over time, indicating that during creep, the GC hydrate transitions to PF hydrate in HBS. The compression of the pore space in HBS under creep conditions (Zhong et al., 2020) may be the main factor, causing an increase in hydrate saturation (Qu et al., 2025). Essentially, as hydrate saturation increases, gas hydrates tend to occur predominantly at the center of the pores (Zhang et al., 2024).

To further validate the accuracy of our proposed model, experimental permeability data from Lu et al. (2019) are compared with the calculated permeability results from the derived model (Fig. 6). To study the evolution of permeability in hydrate-bearing clayey-silt sediment during gas hydrate exploitation via depressurization, Lu et al. (2019) conducted four groups of water seepage experiments under various stress conditions: (I) for the first seepage experiment, $\sigma_1 = 20, 60, 80, 90, 100, 150, 200$ kPa; (II) for the second seepage experiment, $\sigma_1 = 20, 60, 80, 90, 100$ kPa; (III) for the third experiment, $\sigma_1 = 10, 30, 40, 50$ kPa; (IV) for the fourth experiment, $\sigma_1 = 10, 30, 50, 75, 100$ kPa, corresponding to Fig. 6(a)–(d), respectively. The stress loading conditions are adjusted to correspond with the axial stress applied in the experiment during the modeling procedure. The model parameters are set as follows: $\varphi_0 = 0.33$, $S_{h0} = 31\%$, $m = 0.2$, $\theta = \pi/9$, $\alpha = 0.8$, and $t_1 = 60$ h, with additional parameters detailed in Table 5. As depicted in Fig. 6, the predicted permeability does not closely align with the experimental permeability during the early period (0–1200 min), whereas they align well in the later period. Fluctuations in the experimental instruments during the early measurements are responsible for the discrepancy in the initial period. Overall, the proposed model successfully captures the permeability evolution of HBS under creep conditions. Consistent with the results in Figs. 5 and 6 shows that permeability decreases over time even under constant stress. The value of parameter η in Table 5 also illustrates that the hydrate pore morphology changes from GC to PF under creep.

To validate the applicability of the proposed model for predicting the permeability of gas hydrate-bearing sediments in permafrost regions, experimental permeability data from Chuvilin et al. (2025) are compared with the permeability calculated by Eq. (17) (Fig. 7). Chuvilin et al. (2025) measured the gas permeability

Table 1
Parameters for the model validation in Fig. 4(a).

Parameters	F[a] = 1.8 MPa	F[a] = 2.0 MPa	F[a] = 2.2 MPa	F[a] = 2.4 MPa
σ_s[a], MPa	2.2			
G_0[b], MPa	2489	689	2489	2489
K_0[b], MPa	580	480	58	58
G_1[b], MPa	100	70	48	48
G_2[b], MPa	40	40	60	40
H_1[b], MPa·h	42	15	78	78
H_2[b], MPa·h	250	250	250	250
a[b]	0.3	0.15	0.15	0.15
β[b]	1.85	1.85	1.85	1.85

[a] These values are obtained from Sun et al. (2024).
[b] The acceptable range of these values are obtained from Hu et al. (2023).

Table 2
Parameters for the model validation in Fig. 4(b).

Parameters	F[a] = 2.4 MPa	F[a] = 2.6 MPa	F[a] = 2.8 MPa	F[a] = 3.0 MPa
σ_s[a], MPa	2.8			
G_0[b], MPa	2489	2489	3489	2489
K_0[b], MPa	480	580	68	580
G_1[b], MPa	118	130	100	180
G_2[b], MPa	100	100	100	120
H_1[b], MPa·h	18	40	42	82
H_2[b], MPa·h	250	250	250	200
a[b]	0.09	0.22	0.1	0.25
β[b]	1.85	1.85	1.85	3.25

[a] These values are obtained from Sun et al. (2024).
[b] The acceptable range of these values are obtained from Hu et al. (2023).

of gas hydrate-bearing sediment samples from permafrost regions under different axial pressures ($\sigma_1 = 4, 5, 6, 7, 8, 9, 10$ MPa). To be consistent with the experiment, the parameters are set as follows: $\varphi_0 = 0.37$, $S_{h0} = 51\%$, $m = 0.2$, $\theta = \pi/9$ and $\alpha = 0.8$. As can be seen from Fig. 7, the predicted results generally fit well with the experimental data. However, when the axial pressure increases from 6 to 7 MPa, the permeability measured in the experiment drops suddenly, and there is a deviation between the prediction result and the experimental data. A possible reason is that before this axial stress range, the reduction in permeability is caused by the compression of pore space due to effective stress, while at this moment, the phase equilibrium in the pore structure is broken, and the decomposition of hydrates in the pore structure leads to a sudden change in the pore space structure (Chuvilin et al., 2025).

3.2. *Parameter sensitivity analysis*

In this part, to deepen the understanding of the proposed model and supply a theoretical foundation for NGH extraction, a parameter sensitivity analysis is performed to evaluate the effect of key parameters (e.g., S_{h0}, σ_1, m, α, a, and β) on creep strain and permeability of HBS under creep conditions. During the modeling process, the relevant input parameters are set based on Fig. 6(a). Specifically, these parameters are as follows: $\varphi_0 = 0.33$, $S_{h0} = 31\%$, $r_{\max 0} = 5.95$ μm, $m = 0.2$, $\theta = \pi/9$, $\alpha = 0.8$, $t_1 = 40$ h, $a = -6.06 \times 10^{-2}$, $\beta = 3.94$, $\gamma = 0.3$, and $\eta = -1.6$. As illustrated in Fig. 8, the initial hydrate saturation significantly affects both creep strain and permeability. Specifically, a higher initial hydrate saturation leads to a smaller creep strain (Fig. 8(a)). This indicates a clear inverse correlation between initial hydrate saturation and creep strain. This phenomenon can be mechanistically explained by the load-bearing capacity of hydrates within the HBS. As hydrate saturation increases, the hydrate phase assumes a greater proportion of the external load, effectively reinforcing the sediment skeleton (Wu et al., 2023). This reinforcement mechanism enhances the overall stiffness of the sediment system, consequently suppressing creep deformation through improved structural resistance to time-dependent strain. In addition, during HBS creep process, a lower initial hydrate saturation leads to a higher initial permeability and a greater reduction in permeability (Fig. 8(b)). For example, for the HBS with $S_{h0} = 20\%$, the permeability decreases by 24.9% when the time increases from 0 to 40 h, while the permeability with $S_{h0} = 40\%$ decreases by 23.0% within the same time period. The possible reason is that, at lower hydrate saturation, a substantial proportion of pore spaces remain unoccupied, creating more compressible pore spaces in HBS, which in turn causes a more significant reduction in permeability (Yoshimoto and Kimoto, 2022).

Fig. 9 illustrates the impact of ellipsoidal particle aspect ratio α, non-uniform parameter m, dimensionless creep parameter a, related damage parameter β, and axial stress σ_1 on permeability of HBS during creep. As shown in Fig. 9(a), the smaller the aspect ratio of the ellipsoidal sediment particles, the larger the permeability of HBS (when α increases from 0.4 to 1.6, the predicted permeability calculated by Eq. (17) decreases from 33.5 to 18.3 mD in the initial stage of creep). This indicates that, along the flow direction, the permeability of sediments composed of transverse ellipsoidal particles ($\alpha < 1$) is greater than that of longitudinal ellipsoidal particles ($\alpha > 1$). This is because transverse ellipsoidal particles facilitate a looser particle arrangement, creating larger pore spaces and thus higher permeability. Moreover, the smaller aspect ratio α results in a longer a_1 of ellipsoidal particles, forming straighter seepage channels that reduce tortuosity and tortuosity fractal dimension, thereby increasing seepage flow (Xiong et al., 2025). In contrast, longitudinal ellipsoidal particles experience a stacking effect, arranging more tightly, which results in smaller pore space and lower permeability (Song et al., 2024). The relationship illustrated in Fig. 9(b) shows that the smaller the non-uniform parameter m, the more non-uniform the distribution of sediment particles, resulting in a reduced permeability of HBS

Table 3
Parameters for the model validation in Fig. 4(c).

Parameters	F[a] = 2.2 MPa	F[a] = 2.5 MPa	F[a] = 2.8 MPa	F[a] = 3.1 MPa	F[a] = 3.4 MPa	F[a] = 3.7 MPa
σ_s[a], MPa	3.4					
G_0[b], MPa	2489	2489	2489	2489	2489	2489
K_0[b], MPa	650	250	200	190	190	170
G_1[b], MPa	135	150	169	160	160	80
G_2[b], MPa	100	100	100	100	100	100
H_1[b], MPa·h	12	12	12	12	12	12
H_2[b], MPa·h	250	250	250	250	250	250
a[b]	0.08	0.08	0.08	0.08	0.08	0.06
β[b]	1.85	1.85	1.85	1.85	1.85	1.85

[a] These values are obtained from Sun et al. (2024).
[b] The acceptable range of these values are obtained from Hu et al. (2023).

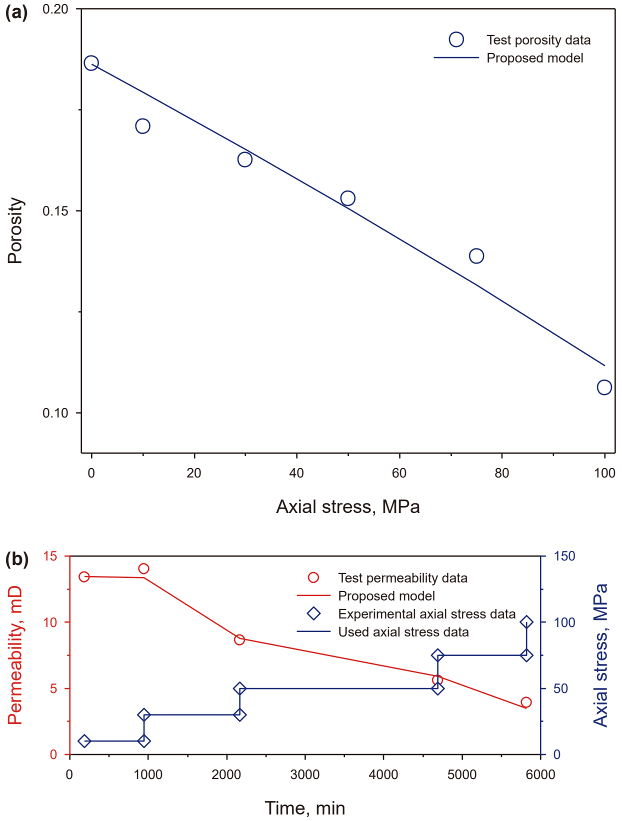

Fig. 5. Comparison of predicted porosity and permeability with experimental data under different stresses ($\sigma_1 = 10$, 30, 50, 75, 100 kPa): **(a)** Porosity; **(b)** Permeability.

(when m increases from 0.1 to 0.8, the predicted permeability increases from 13.4 to 80.4 mD in the initial stage of creep). Additionally, at the same creep time, the closer m is to unit, the greater the increase in permeability. This demonstrates that the non-uniform distribution of sediment particles plays a crucial role in the permeability of HBS. As indicated in Fig. 9(c), during the creep-stable stage (2–34 h), the permeability of HBS is strongly influenced by the dimensionless creep parameter a, with permeability decreasing as the value of parameter a increases. This is due to the fact that, the parameter a in the Kelvin unit of the proposed model indicates the pore structure deformation of HBS during the creep-stable stage. In general, a higher value of parameter a is associated with a greater deformation in the creep-stable stage. Thus, parameter a and the permeability of HBS are negatively related during the creep-stable stage. Similarly, the accelerated creep stage is governed by viscoplastic deformation, characterized by the damage parameter β. In essence, a larger value of parameter β implies a greater pore structure damage of HBS during the acceleration creep stage (17–40 h), resulting in a smaller permeability (Fig. 9(d)). For instance, for a given creep time 40 h, the permeability of HBS decreases from 4.9 to 1.3 mD when the damage parameter β varies from 0.4 to unit. Fig. 9(e) shows that as axial stress increases, the compression of pore space contributes to a reduction in permeability. This reduction becomes more pronounced as the creep time increases, which is expected. For example, when $t = 40$ h, the permeability of HBS decreases from 17.1 to 0.4 mD when the axial stress σ_1 varies from 0.4 to 1.2 MPa. Fig. 9(f) presents a two-factor sensitivity analysis of the aspect ratio α of sediment particles and the non-uniform parameter m. Generally, larger values of m and smaller particle aspect ratio α increase the permeability of the HBS. When the aspect ratio of ellipsoidal particles changes, the extent of permeability reduction corresponding to different m values varies. Specifically, when $m = 0.4$, as α changes from 0.4 to 1.4, the permeability decreases by 90.5%; when $m = 0.1$, as α changes from 0.4 to 1.4, the permeability decreases by 31.9%. At the same particle aspect ratio, increasing the value of m can significantly increase the permeability. For example, when $\alpha = 0.4$, as m changes from 0.1 to 0.2, the permeability increases from 16.9 to 31.5 mD, and as m changes from 0.1 to 0.4, the permeability increases from 16.9 to 221.3 mD. This demonstrates the coupled effect of the aspect ratio α and the non-uniform parameter m on permeability.

Based on the above sensitivity analysis, it can be seen that the particle aspect ratio α, non-uniform parameter m, dimensionless creep parameter a, related damage parameter β, axial stress σ_1, and creep time t have significant effects on the permeability of HBS

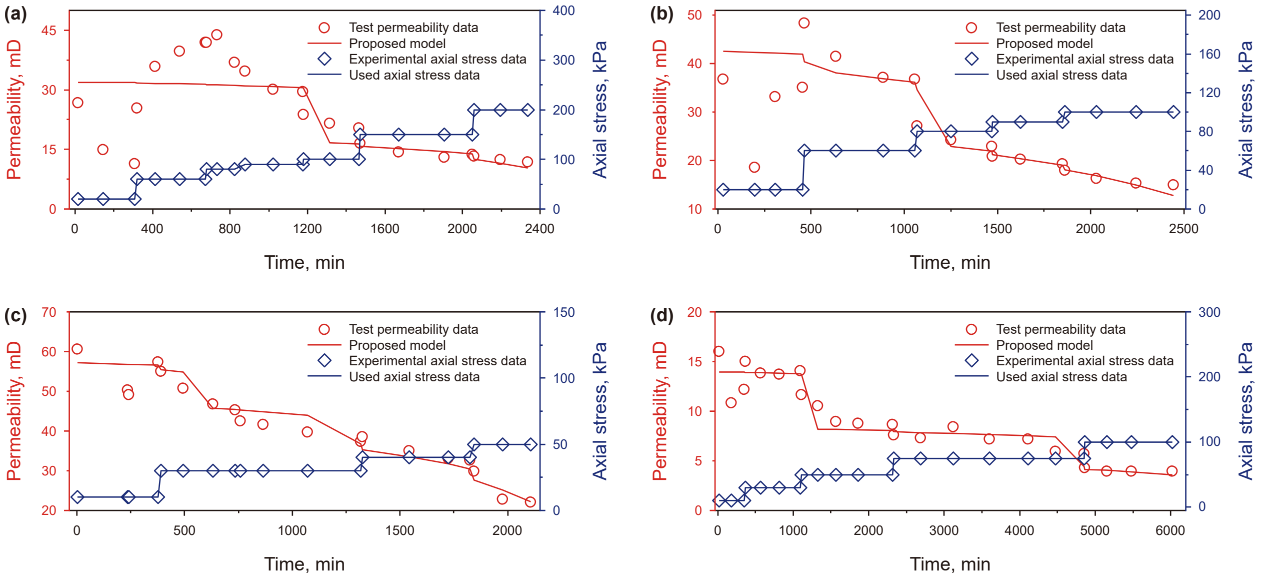

Fig. 6. Comparison of predicted permeability with experimental data under different stresses: **(a)** $\sigma_1 = 20$, 60, 80, 90, 100, 150, 200 kPa; **(b)** $\sigma_1 = 20$, 60, 80, 90, 100 kPa; **(c)** $\sigma_1 = 10$, 30, 40, 50 kPa; **(d)** $\sigma_1 = 10$, 30, 50, 75, 100 kPa.

Table 4
Parameters for the model validation in Fig. 5.

Parameters	G_0[a], MPa	K_0[a], MPa	G_1[a], MPa	G_2[a], MPa	H_1[a], MPa·h	H_2[a], MPa·h	γ[b]	η[b]
Fig. 6(a)	14	350	27	53	1162	637	/	/
Fig. 6(b)	300	583	287	461	1162	450	0.3	−6.4 (0–20 h) −3 (20–80 h) −2.2 (80 h–)

[a] The acceptable range of these values are obtained from Hu et al. (2023).
[b] The reasonable range of these values are obtained from Wang et al. (2021).

Table 5
Parameters for the model validation in Fig. 6.

Parameters	Fig. 6(a)	Fig. 6(b)	Fig. 6(c)	Fig. 6(d)
$r_{\max 0}$[a], μm	5.95	6.2	6.48	4.1
G_0[b], MPa	300	300	300	300
K_0[b], MPa	583	583	583	583
G_1[b], MPa	287	287	287	287
G_2[b], MPa	461	461	65	2615
H_1[b], MPa·h	1162	1162	1162	583
H_2[b], MPa·h	193	35	30	193
a[b] ($\times 10^{-2}$)	−6.06	−6.06	−6.06	−6.06
β[b]	3.94	3.94	3.94	3.94
γ[c]	0.3	0.3	0.3	0.3
η[c]	−3.4 (0–20 h) −1.6 ($t > 20$ h)	−4.3 (0–10 h) −4 (10–20 h) −2.4 ($t > 20$ h)	−6 (0–10 h) −4 (10–20 h) −3.2 ($t > 20$ h)	−5 (0–20 h) −2.4 (20–80 h) −1.3 ($t > 80$ h)

[a] The acceptable range of $r_{\max 0}$ are obtained from Lu et al. (2022) and Xia et al. (2023).
[b] The acceptable range of these values are obtained from Hu et al. (2023).
[c] The acceptable range of these values are obtained from Wang et al. (2021).

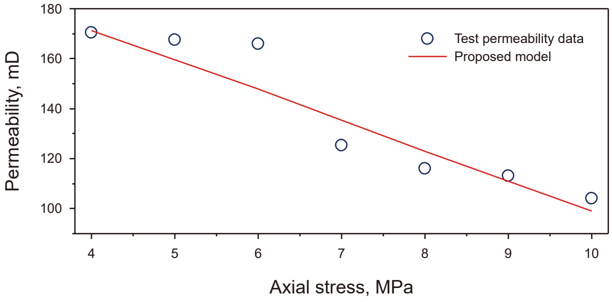

Fig. 7. Comparison of predicted permeability with experimental data tested by Chuvilin et al. (2025) under different stresses: $\sigma_1 = 4, 5, 6, 7, 8, 9, 10$ MPa.

under creep conditions. By performing multiple regression analysis on these six factors, the following empirical equation with a correlation coefficient of 0.992 is obtained.

$$K = 10.014 + 0.071t + m^{2.5} + 13.701\alpha - 10.236a + \beta^{1.5} - 0.444\sigma_1 \tag{18}$$

3.3. Model advantages and limitations

In this work, a creep permeability model for hydrate-bearing sediments (HBS) is developed, taking into account the degree of non-uniform particle distribution, particle shape, pore structure, hydrate saturation and hydrate pore morphology. The proposed model represents sediment particles as ellipsoids, which more

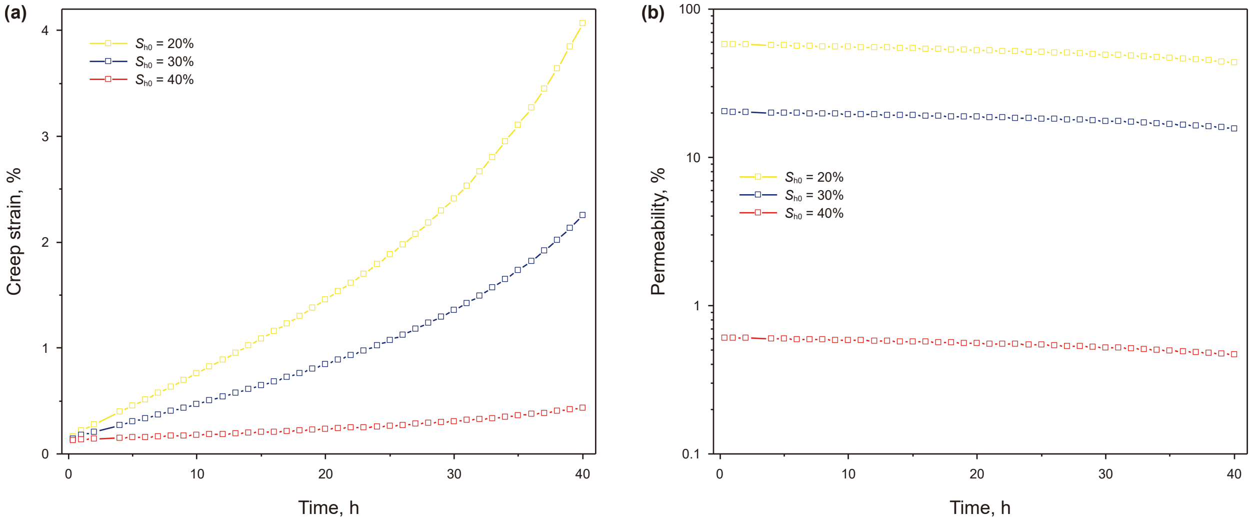

Fig. 8. Impact of initial hydrate saturation on creep strain and permeability: **(a)** Impact on creep strain; **(b)** Impact on permeability.

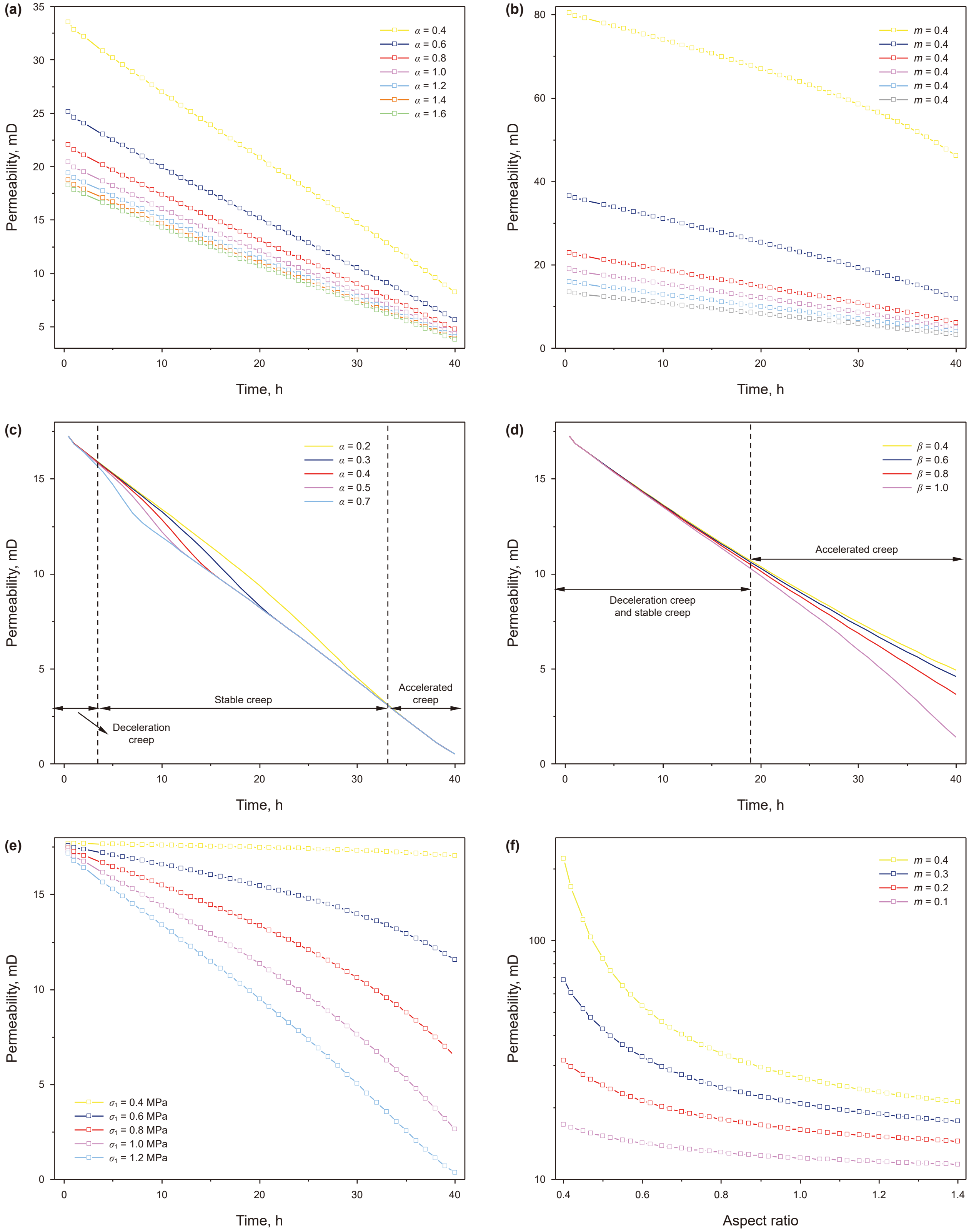

Fig. 9. Impact of axial stress, non-uniform parameter, dimensionless creep parameters, and related damage parameters on permeability: **(a)** Ellipsoidal particle aspect ratio α; **(b)** Non-uniform parameter m; **(c)** Dimensionless creep parameter a; **(d)** Related damage parameter β; and **(e)** axial stress σ_1; **(f)** Aspect ratio α and non-uniform parameter m.

closely resemble natural grain morphology than traditional spherical approximations (Song et al., 2024), thereby providing a more physically realistic representation. Moreover, the proposed model employs non-uniform parameters and offset angles to characterize the non-uniform distribution of sediment particles, which more accurately reflects the real characteristics of the reservoir. Additionally, the proposed model comprehensively considers other factors such as pore structure, hydrate saturation, and hydrate pore morphology, which enables it to more accurately capture the permeability evolution of HBS under various loading conditions compared to former models. Therefore, during the long-term exploitation of natural gas hydrates, the permeability model established in this study can be used to accurately predict the dynamic evolution of permeability under creep, thereby optimizing key mining parameters (such as well spacing and depressurization rate) to effectively avoid engineering risks such as wellbore instability and formation sand production caused by sudden changes in permeability (Li et al., 2025). Additionally, the model can analyze the evolution characteristics of permeability over time to predict the critical conditions for submarine landslide risks, providing key parameters for disaster early warning (Li and Wu, 2022; Gan et al., 2025b).

Despite its contributions, the model has several limitations that warrant further investigation. First, real sediment particles are irregular rather than regularly shaped ellipsoids (Kerimov et al., 2018). To characterize particle shape, more parameters such as sphericity, roundness, and roughness should be used (Wu et al., 2023; Song et al., 2024). Additionally, to avoid complicating the derivation of the theoretical model, the aspect ratio of ellipsoidal particles is used to represent the particle shape. Secondly, although many researchers believe that changes in hydrate saturation can represent hydrate phase transitions (Liu et al., 2019; Zhang et al., 2024), during the long-term exploitation of NGH, hydrate phase transitions are likely to happen near the production wells, involving complex thermodynamic and dynamic behaviors (Kvamme, 2021; Gan et al., 2025a). However, the model proposed in this study only considers changes in hydrate saturation, which is inadequate to fully capture the complexity of these phase transitions. Thirdly, this study only focuses on GC hydrate, PF hydrate and their hybrid morphology. In fact, there are various hydrate morphologies within HBS pore structure, such as cementing and load-bearing, which have also been shown to affect the fluid flow and stiffness of HBS (Sánchez et al., 2017). To further refine our model, other hydrate occurrence patterns will be explored in subsequent research. Finally, sediment particles may undergo breakage under high stress levels (Liao et al., 2024; Hu et al., 2011) (and even under low stress for some soft granular materials (Qian et al., 2024)), but since the average tortuosity model adopted in this paper is derived based on the assumption of intact particles, particle breakage is not considered. This issue is planned to be further explored in future research. Moreover, in future research, we will introduce stress threshold criteria into the creep model to clarify the dominant mechanisms in different stages and improve the dynamic characterization of permeability evolution throughout the entire creep process (Starkova et al., 2011).

4. Conclusions

In this study, a theoretical permeability model for hydrate-bearing sediments (HBS) under creep conditions is developed, incorporating factors such as the degree of non-uniform particle distribution, particle shape, pore structure, hydrate saturation and hydrate pore morphology (including grain-coating, pore-filling and hybrid morphology). The accuracy of the proposed model is verified through comparison with a range of published test data on the permeability of HBS during creep. The key findings of this study are presented below.

(1) Higher initial hydrate saturation results in smaller creep strain and reduces deformation during the accelerated creep phase, thereby enhancing the rigidity and strength of HBS.
(2) The permeability of HBS decreases over time under constant effective stress, with the hydrate pore morphology transitioning from grain-coating to pore-filling during creep.
(3) The aspect ratio α of ellipsoidal sediment particles significantly affects the permeability of HBS, with permeability increasing as the aspect ratio decreases. Permeability is greater under seepage flow parallel to the major axis than under flow parallel to the minor axis.
(4) Non-uniform particle distribution greatly influences the permeability of HBS. Greater non-uniformity results in lower permeability, whereas a more uniform distribution substantially enhances it at the same creep time.
(5) Permeability decreases as the dimensionless creep parameter and the damage parameter increase, due to the creep-stable stage being governed by the Kelvin unit and the acceleration stage being governed by the viscoplastic unit, respectively.

In conclusion, the theoretical permeability model proposed in this work can accurately predict the permeability evolution during the creep process of HBS with various hydrate pore morphologies (grain-coating hydrate, pore-filling hydrate and the hybrid morphology) and non-uniform particle distribution. This research provides theoretical support for the development of natural gas hydrates, which helps optimize the extraction planning and reservoir stability assessments during long-term hydrate exploitation.

CRediT authorship contribution statement

Yi-Han Shang: Writing – original draft, Methodology, Conceptualization. **Gang Lei:** Supervision, Methodology, Investigation, Conceptualization. **Xiao-Yu Yuan:** Validation, Software, Data curation. **Ke-Yi Wang:** Visualization, Software, Formal analysis. **Kai-Xuan Qiu:** Writing – review & editing, Supervision, Methodology.

Data availability

Data will be made available on request.

Declaration of interests

The authors declare that they have no known competing financial interests or personal relationships that could have appeared to influence the work reported in this paper.

Acknowledgements

The authors are grateful for financial support from the National Key Research and Development Program of China (No. 2024YFC2814704), the Natural Science Foundation of Hubei Province, China (No. 2025AFB556), and the Natural Science Foundation of Guangdong Province, China (No. 2024A1515012905).

Nomenclature

Latin symbols

a	Creep parameter (dimensionless)
a_1	Long axes of ellipsoidal particles, μm
a_2	Short axes of ellipsoidal particles, μm
A	Cross-sectional area of REV, cm^2
b_0	Initial center-to-center horizontal distance of two adjacent particles, μm
b	Center-to-center horizontal distance of two adjacent particles, μm
c_0	Initial center-to-center distance of two adjacent particles perpendicular to the flow direction, μm
C	Circumference of the ellipse, μm
D_{f0}	Initial pore fractal dimension (dimensionless)
D_f	Pore fractal dimension under creep (dimensionless)
D_T	Tortuosity fractal dimension (dimensionless)
G_0	Shear modulus for the Hooke element, MPa
G_1	Shear modulus of the modified Kelvin element, MPa
G_2	Shear modulus of the modified viscoplastic element, MPa
H_1	Three-dimensional viscosity coefficient of the modified Kelvin element, MPa·h
H_2	Three-dimensional viscosity coefficient of the modified viscoplastic element, MPa·h
K_0	Bulk modulus for the Hooke element, MPa
K_{PF}	Permeability of HBS with PF hydrate, mD
K_{GC}	Permeability of HBS with GC hydrate, mD
L	Measurement scale of length, cm
m	Non-uniform parameter, dimensionless
ΔP	Pressure drop, MPa
q	Flow rate of a single pipe, cm^3/s
Q_{PF}	Total flow through the cross-section of the REV with PF hydrate, cm^3/s
Q_{GC}	Total flow through the cross-section of the REV with GC hydrate, cm^3/s
r_{max0}	Initial maximum pore radius of HBS, μm
r_{max}	Maximun pore radius of HBS under creep, μm
r_{min0}	Initial minimum pore radius of HBS, μm
r_{min}	Minimum pore radius of HBS under creep, μm
R_0	Initial radius of the spherical particle, μm
r_{PF}	Pore radius with PF hydrate, μm
r_{GC}	Pore radius with GC hydrate, μm
S_{h0}	Initial hydrate saturation of HBS (dimensionless)
S_h	Hydrate saturation of HBS under creep (dimensionless)
t	Creep duration, h
t_1	Damage threshold time, h
V_{b0}	Initial apparent volume, cm^3
V_b	Apparent volume under creep, cm^3
V_{p0}	Initial pore volume, cm^3
V_p	Pore volume under creep, cm^3
ΔV_p	Pore volume of change, cm^3

Greek symbols

α	Aspect ratio of the ellipsoidal particles (dimensionless)
β	Damage-related parameter (dimensionless)
γ	Transitional hydrate saturaton (dimensionless)
σ_1	The first principal stress, MPa
σ_2	The second principal stress, MPa
σ_3	The third principal stress, MPa
σ_s	Long-term strength, MPa
ε_v	Volumetric strain (dimensionless)
θ	Offset angle, °
τ	Average tortuosity (dimensionless)
λ	Pore size of HBS, μm
λ_{min}	Minimum pore size of HBS, μm
λ_{max}	Maximum pore size of HBS, μm
φ	Porosity of HBS under creep (dimensionless)
φ_0	Initial porosity of HBS (dimensionless)
φ_e	Initial effective porosity of HBS (dimensionless)
μ	Fluid dynamic viscosity, Pa·s
η	Evolutional direction of hydrate pore morphology (dimensionless)

Appendix A. Derivation of average tortuosity τ

In this study, the average tortuosity model for hydrate-bearing sediments (HBS) with non-uniform particle distribution is derived based on the model by Peng et al. (2024) under the following assumptions: (I) all particles are identical ellipsoids, with no overlap between particles; (II) the fluid within the HBS is a Newtonian fluid in a laminar flow state. As depicted in Fig. A1(a), the smallest unit of the particle arrangement is represented by yellow lines, with fluid flowing parallel from left to right through adjacent particles within the unit (the red lines represent the fluid paths). Due to the symmetry of the unit structure, a quadrilateral outlined by black dashed lines is used as the calculation model for the average tortuosity, as shown in the enlarged view in Fig. A1(b).

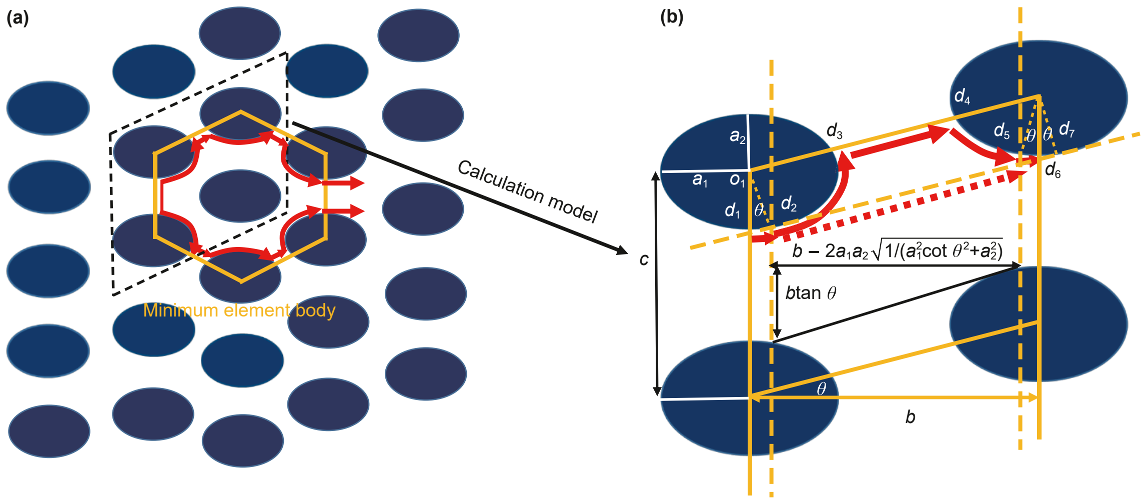

Fig. A1. Schematic diagram of ellipsoidal sediment particle arrangement in HBS: **(a)** Particle position arrangement with a given m and θ; **(b)** The geometric relationship between adjacent particles and assumed flow paths in pore space.

As shown in Fig. A1(b), the aspect ratio of the ellipsoidal particles is obtained as $\alpha = \frac{a_2}{a_1}$ (A1)

where α denotes the aspect ratio of the ellipsoidal particles, a_1 and a_2 are the long and short axes of ellipsoidal particles, respectively.

Regardless of the shape used to represent the sediment particles, the initial porosity of the HBS remains constant, thus the porosity calculated using ellipsoidal sediment particles is equal to that calculated using spherical sediment particles. Therefore, according to the geometric relationship illustrated in Fig. A1(b), the initial porosity of HBS can be expressed as

$$\varphi_0 = \frac{b_0 c_0 - \pi {R_0}^2}{b_0 c_0} = \frac{b_0 c_0 - \pi \alpha a_1^2}{b_0 c_0} \tag{A2}$$

where φ_0 denotes the initial porosity of HBS, b_0 is the initial center-to-center horizontal distance of two adjacent particles in the flow direction, c_0 represents the initial center-to-center distance of two adjacent particles perpendicular to the flow direction, R_0 is the initial radius of the spherical particle. By simplifying Eq. (A2), the following relation can be given as

$$\frac{a_1}{b_0} = \sqrt{\frac{m(1-\varphi_0)}{\alpha \pi}} \tag{A3}$$

where m represents non-uniform parameter, which can be calculated by b_0/c_0. Parameter m characterizes the ratio of the horizontal distance to the vertical distance between adjacent sediment particles. The value of m varies with different types of sediments (Zhang et al., 2024a), when m takes different values, the relative positions of sediment particles change.

As shown in Fig. A1(b), o_1 is the center of the ellipse, d_1, d_3, d_4 and d_6 are the intersection points of the quadrilateral formed at the centers of the four ellipses and the four ellipses respectively, d_2 and d_7 are the tangent points of the common tangent lines to two laterally adjacent ellipses, d_5 is symmetric to d_6. Since the fluid is in laminar flow, the middle region is divided into the longest path $\overset{\frown}{d_2 d_3} + \overline{d_3 d_4} + \overset{\frown}{d_4 d_5}$, and shortest path $\overline{d_2 d_5}$ (Fig. A1(b)), thus the flow path in this region should be represented by the average value, with the typical flow length being b_0.

Based on the geometry of the ellipse, the circumference of the ellipse and the distances from the center of the ellipse to points d_2, d_3 on the ellipse are obtained as

$$C = 2\pi a_2 + 4(a_1 - a_2) \tag{A4}$$

$$\overline{o_1 d_3} = a_1 a_2 \sqrt{\frac{1}{a_1^2 \sin\theta^2 + a_2^2 \cos\theta^2}} \tag{A5}$$

$$\overline{o_1 d_2} = a_1 a_2 \sqrt{\frac{1}{a_1^2 \cos\theta^2 + a_2^2 \sin\theta^2}} \tag{A6}$$

where C represents the circumference of the ellipse, θ represents the offset angle, $\overline{o_1 d_2}$ and $\overline{o_1 d_3}$ represent the distances from the center of the ellipse to points d_2, d_3 on the ellipse, respectively.

The elliptic arc $\overset{\frown}{d_1 d_2}$ and $\overset{\frown}{d_5 d_6}$ are approximated by the length of the arc, which are

$$\overset{\frown}{d_1 d_2} = \overset{\frown}{d_5 d_6} \approx a_2 \theta \tag{A7}$$

where $\overset{\frown}{d_1 d_2}$ and $\overset{\frown}{d_5 d_6}$ are the length of elliptic arcare, respectively.

The longest and shortest paths through the pore space of the fluid in the middle region when the typical flow length being b_0 can be written as

$$\begin{aligned} L_{1,\max} = {} & \frac{1}{2}\left(\overset{\frown}{d_2 d_3} + \overline{d_3 d_4} + \overset{\frown}{d_4 d_5} + \overline{d_2 d_5}\right) + \overset{\frown}{d_1 d_2} + \overset{\frown}{d_5 d_6} = \frac{1}{2} \\ & \left[\begin{gathered} \pi a_2 + 2(a_1 - a_2) - 2a_2\theta + \frac{b_0}{\cos\theta} - 2a_1 a_2 \sqrt{\frac{1}{a_1^2 \sin\theta^2 + a_2^2 \cos\theta^2}} \\ + \sqrt{(b_0 \tan\theta)^2 + \left(b_0 - 2a_1 a_2 \sqrt{\frac{1}{a_1^2 \cot\theta^2 + a_2^2}}\right)^2} \end{gathered} \right] \\ & + 2a_2\theta \end{aligned} \tag{A8}$$

$$L_{1,\min} = \sqrt{(b_0 \tan\theta)^2 + \left(b_0 - 2a_1 a_2 \sqrt{\frac{1}{a_1^2 \cot\theta^2 + a_2^2}}\right)^2} + 2a_2\theta \tag{A9}$$

where $L_{1,\max}$ and $L_{1,\min}$ denote the longest and shortest flow paths when the typical flow length being b_0, respectively.

By combining Eq. (A8) and Eq. (A9), the average path of the fluid is obtained as

$$\begin{aligned} \overline{L}_1 & = \frac{L_{1,\max} + L_{1,\min}}{2} \\ & = \left\{ \begin{gathered} \frac{3}{4}\left[\sqrt{(b_0 \tan\theta)^2 + \left(b_0 - 2a_1 a_2 \sqrt{\frac{1}{a_1^2 \cot\theta^2 + a_2^2}}\right)^2}\right] \\ + \frac{1}{4}\left[\begin{gathered} \pi a_2 + 2(a_1 - a_2) - 2a_2\theta + \frac{b_0}{\cos\theta} \\ -2a_1 a_2 \sqrt{\frac{1}{a_1^2 \sin\theta^2 + a_2^2 \cos\theta^2}} \end{gathered} \right] + 2a_2\theta \end{gathered} \right\} \end{aligned} \tag{A10}$$

where $\overline{L}_1$ is the average flow path when the typical flow length being b_0.

Therefore, the tortuosity τ_1 can be calculated as

$$\tau_1 = \frac{\overline{L_1}}{b_0} \tag{A11}$$

where τ_1 is the tortuosity when the typical flow length being b_0.

According to the model of Peng et al. (2024), if only the middle region is available for flow, the typical flow length becomes $b_0 - 2a_1$, and the tortuosity of HBS should be calculated using the average tortuosity. The longest and shortest paths in the pore space of the fluid can be obtained as

$$\begin{aligned} L_{2,\max} = {} & \frac{1}{2}\left(\overset{\frown}{d_2 d_3} + \overline{d_3 d_4} + \overset{\frown}{d_4 d_5} + \overline{d_2 d_5}\right) + \overset{\frown}{d_1 d_2} + \overset{\frown}{d_5 d_6} = \frac{1}{2} \\ & \left[\begin{gathered} \pi a_2 + 2(a_1 - a_2) - 2a_2\theta + \frac{b_0}{\cos\theta} - 2a_1 a_2 \sqrt{\frac{1}{a_1^2 \sin\theta^2 + a_2^2 \cos\theta^2}} \\ + \sqrt{(b_0 \tan\theta)^2 + \left(b_0 - 2a_1 a_2 \sqrt{\frac{1}{a_1^2 \cot\theta^2 + a_2^2}}\right)^2} \end{gathered} \right] \end{aligned} \tag{A12}$$

$$L_{2,\min} = \sqrt{(b_0 \tan\theta)^2 + \left(b_0 - 2a_1a_2\sqrt{\frac{1}{a_1^2 \cot\theta^2 + a_2^2}}\right)^2} \tag{A13}$$

where $L_{2,\max}$ and $L_{2,\min}$ denote the longest and shortest flow paths when the typical flow length being $b_0 - 2a_1$, respectively.

Then the average path of the fluid can be determined by combining Eq. (A12) and Eq. (A13), which is

$$\begin{aligned} \overline{L}_2 &= \frac{L_{2,\max} + L_{2,\min}}{2} \\ &= \left\{ \begin{array}{l} \dfrac{3}{4}\left[\sqrt{(b_0 \tan\theta)^2 + \left(b_0 - 2a_1a_2\sqrt{\dfrac{1}{a_1^2 \cot\theta^2 + a_2^2}}\right)^2}\right] \\ +\dfrac{1}{4}\left[\begin{array}{l} \pi a_2 + 2(a_1 - a_2) - 2a_2\theta + \dfrac{b_0}{\cos\theta} \\ -2a_1a_2\sqrt{\dfrac{1}{a_1^2 \sin\theta^2 + a_2^2 \cos\theta^2}} \end{array}\right] \end{array} \right\} \end{aligned} \tag{A14}$$

where $\overline{L}_2$ represents the average flow path when the typical flow length being $b_0 - 2a_1$.

The tortuosity τ_2 can be determined by

$$\tau_2 = \frac{\overline{L_2}}{b_0 - 2a_1} \tag{A15}$$

where τ_2 is the tortuosity when the typical flow length being $b_0 - 2a_1$.

Finally, the tortuosity of the HBS composed of ellipsoidal particles can be obtained by averaging Eqs. (A11) and (A15)

$$\tau_{\text{ellipsoid}} = \frac{1}{2}\left(\begin{array}{l} \dfrac{1}{4}\left[1 + \dfrac{1}{1 - 2\sqrt{\alpha}\ \dfrac{a_1}{b_0}}\right]\left[\begin{array}{l} \left(\pi\sqrt{\alpha} - 2\theta - 2\sqrt{\dfrac{\alpha}{\sin\theta^2 + (\alpha\cos\theta)^2}}\right)\alpha\dfrac{a_1}{b_0} \\ +2(1-\alpha)\sqrt{\alpha}\ \dfrac{a_1}{b_0} + \dfrac{1}{\cos\theta} \end{array}\right] + \\ \dfrac{3}{4}\left[1 + \dfrac{1}{1 - 2\sqrt{\alpha}\ \dfrac{a_1}{b_0}}\right]\sqrt{(\tan\theta)^2 + \left(1 - 2\dfrac{a_1}{b_0}\sqrt{\dfrac{\alpha^3}{(\cot\theta)^2 + \alpha^2}}\right)^2} + 2\alpha\dfrac{a_1}{b_0}\theta \end{array} \right) \tag{A16}$$

where $\tau_{\text{ellipsoid}}$ is the average tortuosity of the sediment particles assuming they are ellipsoidal.

When the aspect ratio of the ellipsoidal particle is 1 (i.e., $\alpha = 1$, $a_1 = a_2 = R_0$), the ellipsoidal particles transform into spherical particles, and the average tortuosity calculated using Eq. (A16) is equal to that calculated by Peng et al. (2024).

$$\begin{aligned} &\tau_{\text{ellipsoid}} = \tau_{\text{sphere}} \\ &= \frac{1}{2}\left\{ \begin{array}{l} \dfrac{1}{4}\left[1 + \dfrac{1}{1 - 2\dfrac{R_0}{b_0}}\right]\left[\dfrac{1}{\cos\theta} + (\pi - 2\theta - 2)\dfrac{R_0}{b_0}\right] + 2\dfrac{R_0}{b_0}\theta \\ +\dfrac{3}{4}\left[1 + \dfrac{1}{1 - 2\dfrac{R_0}{b_0}}\right]\left[\sqrt{(\tan\theta)^2 + \left(1 - 2\dfrac{R_0}{b_0}\sin\theta\right)^2}\right] \end{array} \right\} \end{aligned} \tag{A17}$$

where τ_{sphere} is the average tortuosity of the sediment particles assuming they are spherical.

By combining Eqs. (A3) and (A16), the average tortuosity of HBS under creep conditions can be obtained by

$$\begin{array}{l} \tau = \dfrac{1}{8}\left[1 + \dfrac{1}{1 - \sqrt{\dfrac{4m(1-\varphi)}{\pi}}}\right]\left[\begin{array}{l} \left(\pi\sqrt{\alpha} - 2\theta - \sqrt{\dfrac{4\alpha}{\sin\theta^2 + (\alpha\cos\theta)^2}}\right)\sqrt{\dfrac{\alpha m(1-\varphi)}{\pi}} \\ +(1-\alpha)\sqrt{\dfrac{4m(1-\varphi)}{\pi}} + \dfrac{1}{\cos\theta} \end{array}\right] + \\ \dfrac{3}{8}\left[1 + \dfrac{1}{1 - \sqrt{\dfrac{4m(1-\varphi)}{\pi}}}\right]\sqrt{(\tan\theta)^2 + \left(1 - \alpha\sqrt{\dfrac{4m(1-\varphi)}{\left[(\cot\theta)^2 + \alpha^2\right]\pi}}\right)^2} + \sqrt{\dfrac{\alpha m(1-\varphi)}{\pi}}\theta \end{array} \tag{A18}$$

where τ represents the average tortuosity of HBS during creep, φ is the porosity of HBS during creep.

Appendix B. Fractal characteristics of hydrate-bearing sediments

Since the pore structure of HBS satisfies fractal characteristics, when the Euclidean dimension is 2, the initial pore fractal dimension D_{f0} is determined by (Yu and Cheng, 2002; Lei et al., 2019)

$$D_{f0} = 2 - \frac{\ln \varphi_0}{\ln(r_{\min 0}/r_{\max 0})} \tag{B1}$$

where D_{f0} is the initial pore fractal dimension, $r_{\max 0}$ and $r_{\min 0}$ are the initial maximum and minimum pore radius of HBS respectively.

The tortuosity fractal dimension is calculated by (Peng et al., 2024)

$$D_T = 1 + \frac{\ln\left\{\left[\tau\left(D_f + D_T - 1\right)\right]/D_f\right\}}{\ln(L/\lambda_{\min})} \tag{B2}$$

where D_T is the tortuosity fractal dimension, $\lambda_{\min}$ is the minimum pore size of HBS, τ is the average tortuosity of HBS during creep.

The actual length L_t of the capillary is calculated by

$$L_t = \lambda^{1-D_T} L^{D_T} \tag{B3}$$

Based on Yu (2008), the scaling relationship of the cumulative pore number can be described as

$$N(\lambda) = \left(\frac{\lambda_{\max}}{\lambda}\right)^{D_f} \tag{B4}$$

where N denotes cumulative population of pores, $\lambda_{\max}$ is the maximum pore size of HBS. By taking the derivative of Eq. (B4)

$$-\mathrm{d}N = D_f \lambda_{\max}^{D_f} \lambda^{-(D_f+1)} \mathrm{d}\lambda \tag{B5}$$

References

Bhade, P., Phirani, J., 2015. Gas production from layered methane hydrate reservoirs. Energy 82, 686–696. https://doi.org/10.1016/j.energy.2015.01.077.

Cai, J.C., Xia, Y.X., Lu, C., Hang, B., Zou, S.M., 2020. Creeping microstructure and fractal permeability model of natural gas hydrate reservoir. Mar. Petrol. Geol. 115, 104282. https://doi.org/10.1016/j.marpetgeo.2020.104282.

Chen, M.T., Li, Y.L., Zhang, Y.J., Qi, M.H., Wu, N.Y., 2023. Recent advances in creep behaviors characterization for hydrate-bearing sediment. Renew. Sustain. Energy Rev. 183, 113434. https://doi.org/10.1016/j.rser.2023.113434.

Cheng, F.B., Wu, Z.R., Sun, X., Shen, S., Wu, P., Liu, W.G., Chen, B.B., Liu, X.J., Li, Y.H., 2023. Compression-induced dynamic change in effective permeability of hydrate-bearing sediments during hydrate dissociation by depressurization. Energy 264, 126137. https://doi.org/10.1016/j.energy.2022.126137.

Chuvilin, E., Grebenkin, Sergey, Zhmaev, M., 2025. Gas permeability of frozen and hydrate-bearing sediments: experimental evidence. Int. J. Geotech. Eng. 19, 276–286. https://doi.org/10.1080/19386362.2025.2492100.

Danesh, N.N., Chen, Z.W., Aminossadati, S.M., Kizil, M.S., Pan, Z.J., Connell, L.D., 2016. Impact of creep on the evolution of coal permeability and gas drainage performance. J. Nat. Gas Sci. Eng. 33, 469–482. https://doi.org/10.1016/j.jngse.2016.05.033.

Du, P.B., Zhao, C.T., Peng, P., Gao, T., Huang, T., 2020. Fractal characterization of permeability prediction model in hydrate-bearing porous media. Chem. Eng. Sci. 218, 115576. https://doi.org/10.1016/j.ces.2020.115576.

Gajanayake, S.M., Gamage, R.P., Li, X.S., Huppert, H., 2023. Natural gas hydrates – insights into a paradigm-shifting energy resource. Energy Rev. 2, 100013. https://doi.org/10.1016/j.enrev.2022.100013.

Gao, X.W., Lei, G., Zhao, Y.J., Liao, Q.Z., Ning, F.L., 2024. A novel theoretical method for upscaling permeability in hydrate-bearing sediments. Water Resour. Res. 60, e2024WR037729. https://doi.org/10.1029/2024WR037729.

Gan, B., Li, Zhandong, Huo, W., Zhang, Y., Li, Zhong, Fan, R., Zhang, H., Xu, Y., He, Y., 2025a. Phase transitions of CH_4 hydrates in mud-bearing sediments with oceanic laminar distribution: mechanical response and stabilization-type evolution. Fuel 380, 133185. https://doi.org/10.1016/j.fuel.2024.133185.

Gan, B., Li, Zhandong, Zhang, H., Zhang, Y., Huo, W., Li, Zhong, Xu, Y., Li, Y., 2025b. Optimizing hydrate extraction: balancing stability and production efficiency. Fuel 384, 134088. https://doi.org/10.1016/j.fuel.2024.134088.

Guo, Z.H., Vu, P.N.H., Hussain, F., 2018. A laboratory study of the effect of creep and fines migration on coal permeability during single-phase flow. Int. J. Coal Geol. 200, 61–76. https://doi.org/10.1016/j.coal.2018.10.009.

Hafez, A., Liu, Q., Finkbeiner, T., Alouhali, R.A., Moellendick, T.E., Santamarina, J.C., 2021. The effect of particle shape on discharge and clogging. Sci. Rep. 11, 3309. https://doi.org/10.1038/s41598-021-82744-w.

Hu, Q.B., Li, Y.L., Wu, N.Y., Sun, J.X., Chen, Q., Sun, X.F., 2023. Study on creep behaviors and nonlinear creep constitutive model for sandy hydrate-bearing sediments. Ocean Eng. 286, 115717. https://doi.org/10.1016/j.oceaneng.2023.115717.

Hu, Q.B., Sun, X.F., Qu, J.Y., Li, Y.L., 2025. Creep behaviors of methane hydrate-bearing sandy sediments under load-to-unload stress state. Geoenergy Sci. Eng. 247, 213702. https://doi.org/10.1016/j.geoen.2025.213702.

Hu, W., Yin, Z., Dano, C., Hicher, P.-Y., 2011. A constitutive model for granular materials considering grain breakage. Sci. China Technol. Sci. 54, 2188–2196. https://doi.org/10.1007/s11431-011-4491-0.

Katagiri, J., Konno, Y., Yoneda, J., Tenma, N., 2017. Pore-scale modeling of flow in particle packs containing grain-coating and pore-filling hydrates: verification of a Kozeny–Carman-based permeability reduction model. J. Nat. Gas Sci. Eng. 45, 537–551. https://doi.org/10.1016/j.jngse.2017.06.019.

Kerimov, A., Mavko, G., Mukerji, T., Dvorkin, J., Al Ibrahim, M.A., 2018. The influence of convex particles' irregular shape and varying size on porosity, permeability, and elastic bulk modulus of granular porous media: insights from numerical simulations. J. Geophys. Res. Solid Earth 123 (10), 10563–10582. https://doi.org/10.1029/2018JB016031.

Kou, X., Feng, J.C., Li, X.S., Wang, Y., Chen, Z.Y., 2022. Formation mechanism of heterogeneous hydrate-bearing sediments. Appl. Energy 326, 119931. https://doi.org/10.1016/j.apenergy.2022.119931.

Kvamme, B., 2021. Kinetics of hydrate formation, dissociation and reformation. Chem. Thermodyn. Therm. Anal. 1–2, 100004. https://doi.org/10.1016/j.ctta.2021.100004.

Lai, J., Wang, G.W., Wang, Z.Y., Chen, J., Pang, X.J., Wang, S.C., et al., 2018. A review on pore structure characterization in tight sandstones. Earth Sci. Rev. 177, 436–457. https://doi.org/10.1016/j.earscirev.2017.12.003.

Lei, G., Cao, N., Liu, D., Wang, H.J., 2018a. A non-linear flow model for porous media based on conformable derivative approach. Energies 11, 2986. https://doi.org/10.3390/en11112986.

Lei, G., Dong, Z.Z., Li, W.R., Wen, Q.Z., Wang, C., 2018b. Theoretical study on stress sensitivity of fractal porous media with irreducible water. Fractals 26, 1850004. https://doi.org/10.1142/S0218348X18500044.

Lei, G., Liao, Q.Z., Patil, S., 2019. A fractal model for relative permeability in fractures under stress dependence. Fractals 27, 1950092. https://doi.org/10.1142/S0218348X19500920.

Lei, G., Liao, Q., Patil, S., Zhao, Y., 2021. A new permeability model for argillaceous porous media under stress dependence with clay swelling. Int. J. Eng. Sci. 160, 103452. https://doi.org/10.1016/j.ijengsci.2020.103452.

Lei, G., Liao, Q., Zhang, D.X., Patil, S., 2020. A mechanistic model for permeability in deformable gas hydrate-bearing sediments. J. Nat. Gas Sci. Eng. 83, 103554. https://doi.org/10.1016/j.jngse.2020.103554.

Lei, G., Qu, J.T., Zhao, Y.J., Wu, Q., Liu, T.L., 2024a. Permeability behavior of hydrate-bearing clayey-silty sediments during creeping. J. Rock Mech. Geotech. Eng. https://doi.org/10.1016/j.jrmge.2024.04.014.

Lei, G., Tang, J.D., Zhang, L., Wu, Q., Li, J., 2024b. Effective thermal conductivity for hydrate-bearing sediments under stress and local thermal stimulation conditions: A novel analytical model. Energy 288, 129704. https://doi.org/10.1016/j.energy.2023.129704.

Lei, L., Gai, X.R., Seol, Y., 2020. Load-bearing characteristic of methane hydrate within coarse-grained sediments – insights from isotropic consolidation. Mar. Petrol. Geol. 121, 104571. https://doi.org/10.1016/j.marpetgeo.2020.104571.

Li, C.H., Zhao, Q., Xu, H.J., Feng, K., Liu, X.W., 2014. Relation between relative permeability and hydrate saturation in Shenhu area, South China Sea. Appl. Geophys. 11, 207–214. https://doi.org/10.1007/s11770-014-0432-6.

Li, H.C., Li, J.H., Li, L., Li, Z.D., 2024. Predicting turbidite channel in deep-water canyon based on grey relational analysis-support vector machine model: a case study of the Lingshui depression in Qiongdongnan Basin, South China Sea. Energy 121, 2435–2447. https://doi.org/10.32604/ee.2024.050771.

Li, Q.C., Cheng, Y.F., Li, Q., Ansari, U., Liu, Y.W., Yan, C.L., Lei, C., 2018. Development and verification of the comprehensive model for physical properties of hydrate sediment. Arabian J. Geosci. 11, 325. https://doi.org/10.1007/s12517-018-3685-1.

Li, Q.C., Wu, J.J., 2022. Factors affecting the lower limit of the safe mud weight window for drilling operation in hydrate-bearing sediments in the Northern South China Sea. Geomech. Geophys. Geo-energ. Geo-resour. 8, 82. https://doi.org/10.1007/s40948-022-00396-0.

Li, Q.C., Wu, J.J., L, Q., W, F.L., C, Y.F., 2025. Sediment instability caused by gas production from hydrate-bearing sediment in Northern South China Sea by horizontal wellbore: Sensitivity analysis. Nat. Resour. Res. 34, 1667–1699. https://doi.org/10.1007/s11053-025-10478-x.

Li, R.R., Zhang, L.Q., Zhou, J., Han, Z.H., Pan, Z.J., Schüttrumpf, H., 2023. Investigation on permeability anisotropy in unconsolidated hydrate-bearing sediments based on pore-scale numerical simulation: effect of mineral particle shape and pore-filling. Energy 267, 126456. https://doi.org/10.1016/j.energy.2022.126456.

Li, Y., Cheng, Y.F., Yan, C.L., Wang, Z.Y., Song, L.F., 2022. Effects of creep characteristics of natural gas hydrate-bearing sediments on wellbore stability. Pet. Sci. 19, 220–233. https://doi.org/10.1016/j.petsci.2021.10.026.

Li, Y.H., Liu, W.G., Song, Y.C., Yang, M.J., Zhao, J.F., 2016. Creep behaviors of methane hydrate coexisting with ice. J. Nat. Gas Sci. Eng. 33, 347–354. https://doi.org/10.1016/j.jngse.2016.05.042.

Li, Y.H., Wu, P., Sun, X., Liu, W.G., Song, Y.C., Zhao, J.F., 2019. Creep behaviors of methane hydrate-bearing frozen sediments. Energies 12, 251. https://doi.org/10.3390/en12020251.

Li, Z.D., Gan, B.C., Li, Z., Zhang, H.X., Wang, D.J., Zhang, Y.Z., Wang, Y.A., 2023. Kinetic mechanisms of methane hydrate replacement and carbon dioxide hydrate reorganization. Chem. Eng. J. 477, 146973. https://doi.org/10.1016/j.cej.2023.146973.

Liao, D., Wang, S., Zhang, C., 2024. A hypoplastic model for crushable sand under a wide range of stress levels. Acta Geotech 19, 5465–5480. https://doi.org/10.1007/s11440-024-02230-1.

Lin, Z.Z., Dong, H.M., Pan, H.P., Sun, J.M., Fang, H., Wang, X.J., 2019. Study on the equivalence between gas hydrate digital rocks and hydrate rock physical models. J. Pet. Sci. Eng. 181, 106241. https://doi.org/10.1016/j.petrol.2019.106241.

Liu, J.W., Li, X.S., 2021. Recent advances on natural gas hydrate exploration and development in the South China Sea. Energy Fuel 35, 7528–7552. https://doi.org/10.1021/acs.energyfuels.1c00494.

Liu, L.L., Dai, S., Ning, F.L., Cai, J.C., Liu, C.L., Wu, N.Y., 2019. Fractal characteristics of unsaturated sands – implications to relative permeability in hydrate-bearing sediments. J. Nat. Gas Sci. Eng. 66, 11–17. https://doi.org/10.1016/j.jngse.2019.03.019.

Liu, T., Wu, P., Lu, Q.Y., Li, Y.H., Song, Y.C., 2024. Creep and wave velocity characterization on anisotropic consolidated methane hydrate sediments of the South China Sea. Energy Fuel 38, 16416–16425. https://doi.org/10.1021/acs.energyfuels.4c02845.

Liu, X.L., Li, D.J., Han, C., 2020. A nonlinear damage creep model for sandstone based on fractional theory. Arab. J. Geosci. 13, 246. https://doi.org/10.1007/s12517-020-5215-1.

Liu, Y.F., Liu, Y.T., Sun, L., Liu, J., 2016. Multiscale fractal characterization of hierarchical heterogeneity in sandstone reservoirs. Fractals-complex geom. Patterns Scaling Nat. Soc. 24, 1650032. https://doi.org/10.1142/S0218348X16500328.

Liu, Y.F., Jeng, D.S., 2019. Pore scale study of the influence of particle geometry on soil permeability. Adv. Water Resour. 129, 232–249. https://doi.org/10.1016/j.advwatres.2019.05.024.

Lu, C., Xia, Y.X., Qin, X.W., Ma, C., Bian, H., Xing, D.H., Lu, H.F., 2022. Micro- and nanoscale pore structure characterization and mineral composition analysis of clayey-silt hydrate reservoir in South China Sea. Geofluids 2022, 2837193. https://doi.org/10.1155/2022/2837193.

Lu, C., Xia, Y.X., Sun, X.X., Bian, H., Qiu, H.J., Lu, H.F., Luo, W.J., Cai, J.C., 2019. Permeability evolution at various pressure gradients in natural gas hydrate reservoir at the shenhu area in the South China Sea. Energies 12, 3688. https://doi.org/10.3390/en12193688.

Luo, H.L., Jougnot, D., Jost, A., Teng, J.D., Thanh, L.D., 2023. A capillary bundle model for the electrical conductivity of saturated frozen porous media. J. Geophys. Res. Solid Earth 128, e2022JB025254. https://doi.org/10.1029/2022JB025254.

Lv, J.C., Xue, K.P., Zhang, Z.D., Cheng, Z.C., Liu, Y., Mu, H.L., 2021. Pore-scale investigation of hydrate morphology evolution and seepage characteristics in hydrate bearing microfluidic chip. J. Nat. Gas Sci. Eng. 88, 103881. https://doi.org/10.1016/j.jngse.2021.103881.

Mahabadi, N., Dai, S., Seol, Y., Jang, J., 2019. Impact of hydrate saturation on water permeability in hydrate-bearing sediments. J. Pet. Sci. Eng. 174, 696–703. https://doi.org/10.1016/j.petrol.2018.11.084.

Mao, M.H., Yan, K.F., Li, X.S., Chen, Z.Y., Wang, Y., Feng, J.C., Chen, C., 2024. Review of heat transfer characteristics of natural gas hydrate. Energies 17, 717. https://doi.org/10.3390/en17030717.

Miyazaki, K., Tenma, N., Yamaguchi, T., 2017. Relationship between creep property and loading-rate dependence of strength of artificial methane-hydrate-bearing toyoura sand under triaxial compression. Energies 10, 1466. https://doi.org/10.3390/en10101466.

Miyazaki, K., Yamaguchi, T., Sakamoto, Y., Aoki, K., 2011. Time-dependent behaviors of methane-hydrate bearing sediments in triaxial compression test. Int. J. JCRM. 7, 43–48. https://doi.org/10.11187/ijjcrm.7.43.

Ouria, A., 2024. Coupled creep and nonlinear consolidation of soft soils in disturbed state concept framework. Comput. Geotech. 166, 105955. https://doi.org/10.1016/j.compgeo.2023.105955.

Peng, H., Li, X.S., Chen, Z.Y., Ji, H.F., Zhang, Y., You, C.Y., 2024. Nonempirical fractal permeability model and experimental verification of hydrate-bearing sediments based on heterogeneous distribution of particles. Geoenergy Sci. Eng. 237, 212773. https://doi.org/10.1016/j.geoen.2024.212773.

Qian, H., Xu, C., Wu, W., Du, X., 2024. A hypoplastic model considering grain breakage and wetting effect for granular material. Comput. Geotech. 171, 106329. https://doi.org/10.1016/j.compgeo.2024.106329.

Qu, J.T., Lei, G., Liu, T.L., Sun, J.X., Zheng, S.J., Qu, B., 2024. Theoretical investigation of threshold pressure gradient in hydrate-bearing clayey-silty sediments under combined stress and local thermal stimulation conditions. Gas Sci. Eng. 129, 205418. https://doi.org/10.1016/j.jgsce.2024.205418.

Qu, J.T., Liu, T.L., Lei, G., Zheng, S.J., Cheng, W., Sun, J.X., Wan, Y.Z., 2025. A model for threshold pressure gradient in hydrate-bearing sediments during creep. J. Rock Mech. Geotech. Eng. https://doi.org/10.1016/j.jrmge.2024.10.029.

Ren, X.W., Guo, Z.Y., Ning, F.L., Ma, S.Z., 2020. Permeability of hydrate-bearing sediments. Earth Sci. Rev. 202, 103100. https://doi.org/10.1016/j.earscirev.2020.103100.

Sánchez, M., Gai, X.R., Santamarina, J.C., 2017. A constitutive mechanical model for gas hydrate bearing sediments incorporating inelastic mechanisms. Comput. Geotech. 84, 28–46. https://doi.org/10.1016/j.compgeo.2016.11.012.

Song, H.H., Xie, J.L., Yin, P.J., Fu, H.Z., Zhang, Y., Yan, C.G., 2024. The investigation of the particle shape effect on the permeability of porous media through lattice Boltzmann simulation and experimental study. Int. J. Therm. Sci. 201, 108983. https://doi.org/10.1016/j.ijthermalsci.2024.108983.

Starkova, O., Papanicolaou, G.C., Xepapadaki, A.G., Aniskevich, A., 2011. A method for determination of time- and temperature-dependences of stress threshold of linear–nonlinear viscoelastic transition: energy-based approach. J. Appl. Polym. Sci. 121, 2187–2192. https://doi.org/10.1002/app.33813.

Sun, S.H., Zhang, X.H., Zhou, Y.J., 2024. Features and constitutive model of hydrate-bearing sandy sediment's triaxial creep failure. Water 16, 2947. https://doi.org/10.3390/w16202947.

Tang, J.D., Lei, G., Li, X.D., Zhang, L., Cheng, W., Pang, J.T., Jiang, G.S., 2023. A novel analytical model of the effective thermal conductivity of porous materials under stress. Fractals 31, 2340176. https://doi.org/10.1142/S0218348X2340176X.

Tang, J.D., Lei, G., Wu, Q., Zhang, L., Ning, F.L., 2024. An improved analytical model of effective thermal conductivity for hydrate-bearing sediments during elastic-plastic deformation and local thermal stimulation. Energy 305, 132293. https://doi.org/10.1016/j.energy.2024.132293.

Tickell, F.G., Hiatt, W.N., 1938. Effect of angularity of grain on porosity and permeability of unconsolidated sands: geological NOTES1. AAPG Bull. 22, 1272–1274. https://doi.org/10.1306/3D932FF0-16B1-11D7-8645000102C1865D.

Wang, L., Shen, S., Wu, Z.R., Wu, D.J., Li, Y.H., 2024. Strength and creep characteristics of methane hydrate-bearing clayey silts of the South China Sea. Energy 294, 130789. https://doi.org/10.1016/j.energy.2024.130789.

Wang, Q.L., Chen, X.Y., Zhang, L.X., Wang, Z.M., Wang, D.Y., Dai, S., 2021. An analytical model for the permeability in hydrate-bearing sediments considering the dynamic evolution of hydrate saturation and pore morphology. Geophys. Res. Lett. 48, e2021GL093397. https://doi.org/10.1029/2021GL093397.

Wang, Y.H., Wu, P., Huang, L., Song, Y.C., Li, Y.H., 2025. Stress-induced permeability evolution mechanism of hydrate-bearing sediments from pore-scale perspective. Energy 319, 134977. https://doi.org/10.1016/j.energy.2025.134977.

Washburn, E.W., 1921. The dynamics of capillary flow. Phys. Rev. 17, 273–283. https://doi.org/10.1103/PhysRev.17.273.

Wu, P., Wang, H.J., Huang, L., Liu, T., Li, Y.H., 2023. Pore-scale analysis of hydrate saturation on the physical parameters of hydrate-bearing sediment with different particle shapes. Gas Sci. Eng. 116, 205052. https://doi.org/10.1016/j.jgsce.2023.205052.

Wu, Z.R., Yang, S.H., Liu, W.G., Li, Y.H., 2022. Permeability analysis of gas hydrate-bearing sand/clay mixed sediments using effective stress laws. J. Nat. Gas Sci. Eng. 97, 104376. https://doi.org/10.1016/j.jngse.2021.104376.

Xia, Y.X., Xu, S., Lu, C., Andersen, P.Ø., Cai, J.C., 2023. Characterization and capillary pressure curve estimation of clayey-silt sediment in gas hydrate reservoirs of the South China Sea. Adv. Geo-Energy Res. 10, 200–207. https://doi.org/10.46690/ager.2023.12.06.

Xiong, B.B., Kuang, R., Zhang, P., Tian, B., Gao, H.H., Zheng, Q., Li, Y.Q., 2025. Effect of particle size, sphericity, and distribution on seepage in granular porous media. Geotech. Geol. Eng. 43, 131. https://doi.org/10.1007/s10706-025-03095-1.

Yan, B.Q., Guo, Q.F., Ren, F.H., Cai, M.F., 2020. Modified Nishihara model and experimental verification of deep rock mass under the water-rock interaction. Int. J. Rock Mech. Min. Sci. 128, 104250. https://doi.org/10.1016/j.ijrmms.2020.104250.

Yang, D.Z., Chu, X.H., 2024. Influence of particle shape on creep and stress relaxation behaviors of granular materials based on DEM. Comput. Geotech. 166, 105941. https://doi.org/10.1016/j.compgeo.2023.105941.

Yoneda, J., Oshima, M., Kida, M., Kato, A., Konno, Y., Jin, Y., Tenma, N., 2019. Consolidation and hardening behavior of hydrate-bearing pressure-core sediments recovered from the Krishna–Godavari basin, offshore India. Mar. Petrol. Geol. 108, 512–523. https://doi.org/10.1016/j.marpetgeo.2018.09.021.

Yoshimoto, M., Kimoto, S., 2022. Undrained creep behavior of CO_2 hydrate-bearing sand and its constitutive modeling considering the cementing effect of hydrates. Soils Found 62, 101095. https://doi.org/10.1016/j.sandf.2021.101095.

Yu, B.M., 2008. Analysis of flow in fractal porous media. Appl. Mech. Rev. 61. https://doi.org/10.1115/1.2955849.

Yu, B.M., Cheng, P., 2002. A fractal permeability model for bi-dispersed porous media. Int. J. Heat Mass Tran. 45, 2983–2993. https://doi.org/10.1016/S0017-9310(02)00014-5.

Yu, B.M., Li, J.H., 2001. Some fractal characters of porous media. Fractals 9, 365–372. https://doi.org/10.1142/S0218348X01000804.

Zhang, N., Wang, H.N., Jiang, M.J., 2024. A mechanistic model for porosity and permeability in deformable hydrate-bearing sediments with various hydrate growth patterns. Acta Geotech 19, 855–880. https://doi.org/10.1007/s11440-023-01954-w.

Zhang, Y.C., Liu, L.L., Li, J., Chen, Q., Li, C.F., Sun, J.Y., Liu, C.L., 2024a. The pore-structure characteristics of foraminiferal shells and their relations with natural gas hydrate formation in the marine sediments. Gas Sci. Eng. 124, 205257. https://doi.org/10.1016/j.jgsce.2024.205257.

Zhang, Y.C., Liu, L.L., Sun, J.Y., Li, C.F., Wan, Y.Z., Ji, Y.K., Chen, Q., Liu, C.L., Wu, N.Y., 2024b. Application of time domain reflectometry to triaxial shear tests on hydrate-bearing sediments. Measurement 238, 115369. https://doi.org/10.1016/j.measurement.2024.115369.

Zhang, Z., Li, C.F., Ning, F.L., Liu, L.L., Cai, J.C., Liu, C.L., Wu, N.Y., Wang, D.G., 2020. Pore fractal characteristics of hydrate-bearing sands and implications to the saturated water permeability. J. Geophys. Res. Solid Earth 125, e2019JB018721. https://doi.org/10.1029/2019JB018721.

Zhang, Z., Liu, L.L., Ning, F.L., Liu, Z.C., Sun, J.Y., Li, X.D., Sun, J.X., Hyodo, M., Liu, C.L., 2022. Effect of stress on permeability of clay silty cores recovered from the Shenhu hydrate area of the South China Sea. J. Nat. Gas Sci. Eng. 99, 104421. https://doi.org/10.1016/j.jngse.2022.104421.

Zhong, X.Y., Zhu, Y.S., Liu, L.P., Yang, H.M., Li, Y.F., Xie, Y.H., Liu, L.Y., 2020. The characteristics and influencing factors of permeability stress sensitivity of tight sandstone reservoirs. J. Pet. Sci. Eng. 191, 107221. https://doi.org/10.1016/j.petrol.2020.107221.